iScience

Article

A Genetic modification that reduces ON-bipolar cells in hESC-derived retinas enhances functional integration after transplantation

Differentiation

Islet-1⁻ᐟ⁻ hESC-retina

Transplantation

Islet-1⁻ᐟ⁻ hESC

RD-nude rat eye

Wild type hESC-retina Transplantation

Islet-1⁻ᐟ⁻ hESC-retina Transplantation (reduced bipolar cells)

Better host-graft contact

Better RGC light responsiveness

Suguru Yamasaki,
Hung-Ya Tu, Take
Matsuyama, ...,
Toru Kimura,
Masayo
Takahashi,
Michiko Mandai

michiko.mandai@riken.jp

Highlights

Deletion of *ISL1* in hESC-retinas resulted in a reduced number of ON-bipolar cells

Photoreceptors in $ISL1^{-/-}$ hESC-retinas achieved functional maturation *in vivo*

$ISL1^{-/-}$ hESC-retinas showed better host-graft contact with putative synapses

$ISL1^{-/-}$ hESC-retinas better restored RGC light responsiveness in degenerated retina
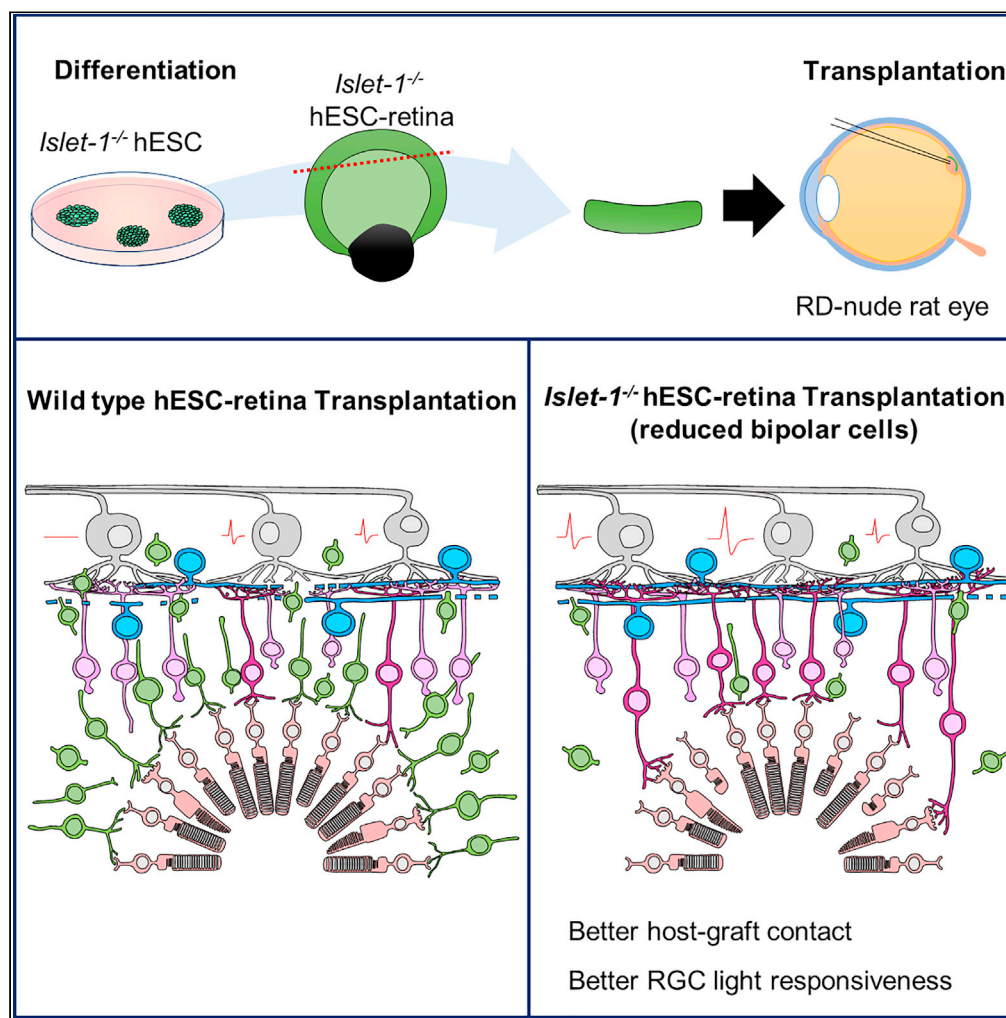
Article

A Genetic modification that reduces ON-bipolar cells in hESC-derived retinas enhances functional integration after transplantation

Suguru Yamasaki,[1,2] Hung-Ya Tu,[1,3] Take Matsuyama,[1,4] Matsuri Horiuchi,[1,2] Tomoyo Hashiguchi,[1] Junki Sho,[1] Atsushi Kuwahara,[2] Akiyoshi Kishino,[2] Toru Kimura,[2] Masayo Takahashi,[1] and Michiko Mandai[1,4,5,6,*]

SUMMARY

Pluripotent stem cell (PSC)-derived retinal sheet transplanted *in vivo* can form structured photoreceptor layers, contact with host bipolar cells, and transmit light signals to host retinas. However, a major concern is the presence of graft bipolar cells that may impede host-graft interaction. In this study, we used human ESC-retinas with the deletion of *Islet-1* (*ISL1*) gene to achieve the reduced graft ON-bipolar cells after xenotransplantation into end-stage retinal degeneration model rats. Compared with wild-type graft, *ISL1*$^{-/-}$ hESC-retinas showed better host-graft contact, with indication of host-graft synapse formation and significant restoration of light responsiveness in host ganglion cells. We further analyzed to find out that improved functional integration of *ISL1*$^{-/-}$ hESC-retinas seemed attributed by a better host-graft contact and a better preservation of host inner retina. *ISL1*$^{-/-}$ hESC-retinas are promising for the efficient reconstruction of a degenerated retinal network in future clinical application.

INTRODUCTION

Photoreceptor cell replacement therapy for retinal degenerative diseases including retinitis pigmentosa (RP) and age-related macular degeneration (AMD) is considered an attractive approach to restore visual function. The advance of innovative technology to generate self-organizing retinal organoids from mouse and human embryonic stem cells (ESCs) or induced pluripotent stem cells (iPSCs) enabled retinal tissue transplantation for end-stage retinal degeneration, with a stable supply of retinal cells that are qualitatively comparable with fetal retinal tissue or cells (Eiraku et al., 2011; Kuwahara et al., 2015, 2019; Meyer et al., 2009; Nakano et al., 2012; Reichman et al., 2014; Zhong et al., 2014). Transplantation of hESC/iPSC-retinal tissue-sheet (retinal sheet, here after) or cells has been conducted in animal models of end-stage retinal degeneration to show functional potential to elicit light responses in host retinal ganglion cells (RGC) and light-guided behaviors (Iraha et al., 2018; Mandai et al., 2017; McLelland et al., 2018; Ribeiro et al., 2021; Tu et al., 2019; Zerti et al., 2021). Based on these proof-of-concept studies, we recently initiated the first-in-human clinical research to confirm the safety of hiPSC-retinal sheet transplantation in patients with RP.

Photoreceptor transplantation into the subretinal space can be conducted either in the form of a cell suspension or as retinal sheet. In the end-stage host retina, transplantation of purified photoreceptors is advantageous in forming direct contact with host bipolar cells, whereas retinal sheet transplantation is reported to be associated with longer graft survival, low immunogenicity, and photoreceptor maturation with a layered structure with formation of outer segments (OS)-like structures as also confirmed by electron microscopy (Assawachananont et al., 2014; Iraha et al., 2018; Shirai et al., 2016; Tu et al., 2019; Yamasaki et al., 2021). However, the ESC/iPSC-retinal sheet also provides retinal inner cells, which may simultaneously benefit and hinder the host-graft integration. Müller glia are important for the development of OS structures, glutamate uptake, and recycling of visual pigments, mostly for cone photoreceptors (Bringmann et al., 2009; Wang and Kefalov, 2011). Horizontal cells participate in ribbon synapses and contribute to the integration and regulation of the signals from photoreceptors, and the deletion of horizontal cells leads to photoreceptor degeneration (Janssen-Bienhold et al., 2012). On the other hand, bipolar cells in the retinal sheet seemed to impede host bipolar cells contacting and forming synapses with graft photoreceptors (Assawachananont et al., 2014).

[1]Laboratory for Retinal Regeneration, RIKEN Center for Biosystems Dynamics Research, Kobe 650-0047, Japan

[2]Regenerative & Cellular Medicine Kobe Center, Sumitomo Dainippon Pharma Co., Ltd., Kobe 650-0047, Japan

[3]Laboratory for Molecular and Developmental Biology, Institute for Protein Research, Osaka University, Osaka 565-0871, Japan

[4]Department of Ophthalmology, Kobe City Eye Hospital, Kobe 650-0047, Japan

[5]RIKEN Program for Drug Discovery and Medical Technology Platforms (DMP), RIKEN Cluster for Science, Technology and Innovation Hub., Saitama, 351-0198, Japan

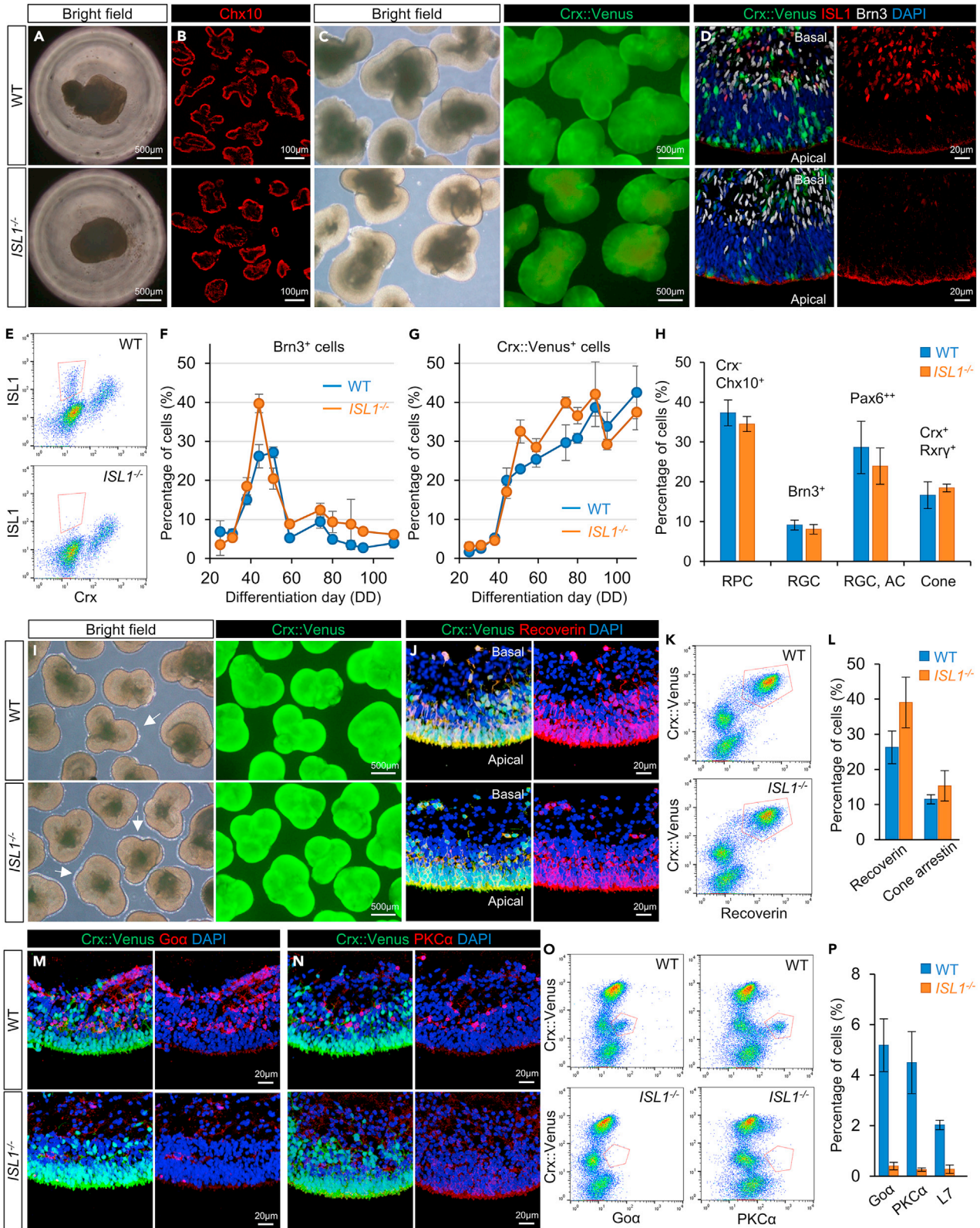[6]Lead contact

*Correspondence: michiko.mandai@riken.jp

https://doi.org/10.1016/j.isci.2021.103657

Figure 1. Retinal differentiation from $ISL1^{-/-}$ hESC

(A) Bright field image of WT and $ISL1^{-/-}$ hESC-retinas showing the aggregation on 96 well V-plate (DD15).

(B) Immunostaining of the DD15 WT and $ISL1^{-/-}$ hESC-retina for expressed Chx10.

(C) At DD88, self-organized retinas with a continuous epithelial structure were consistently differentiated from WT and $ISL1^{-/-}$ hESC with $Crx::Venus$ expression.

(D) WT and $ISL1^{-/-}$ hESC-retinas were stained with ISL1 and Brn3 (DD60).

(E) FCM analysis of ISL1 and Crx population on WT and $ISL1^{-/-}$ hESC-retina (DD54).

(F and G) Temporal population changes in Brn3$^+$ RGCs and $Crx::Venus^+$ photoreceptors of WT (blue) and $ISL1^{-/-}$ (orange) hESC-retinas quantified by FCM (n = 3 for each).

(H) Population of RPC (Crx$^-$/Chx10$^+$), RGC (Brn3$^+$), RGC and AC (Pax6^{++}), and cone photoreceptors (Crx$^+$/Rxrγ$^+$) in WT and $ISL1^{-/-}$ hESC-retina quantified by FCM at DD58 (n = 4 for each).

(I) $Crx::Venus^+$ hESC-retinas with cilia-like structures on the surface in long-term culture at DD235 (arrows).

(J–P) Representative immunostaining and FACS plot for WT and $ISL1^{-/-}$ hESC-retinas at around DD240. (J–L) Photoreceptors formed ONL-like structure with a similar differentiation rate of photoreceptors. (M–P) ON/rod-bipolar cell populations with PKCα, L7, and Goα expression were diminished in $ISL1^{-/-}$ hESC-retina (n = 3 for each). Data are presented as means ± SEM.

Based on these observations, in order to enhance host-graft contact by reducing graft bipolar cells while retaining the cellular and structural benefits of the retinal sheet, we recently reported the knockout (KO) effect of *Bhlhb4* and *Islet-1 (Isl1)* genes that are related to the fate-determination and maturation of bipolar cells, in mouse ESC/iPSC-retinal sheet (Matsuyama et al., 2021). Previous studies showed that *Bhlhb4* gene deletion specifically reduced rod bipolar cells (Bramblett et al., 2004), whereas *Isl1* conditional KO mice presented a considerable reduction of ON-bipolar cells, cholinergic amacrine cells, and RGC (Elshatory et al., 2007). Consistently, using mouse ESC/iPSC-retinas, we observed a drastic reduction of rod bipolar cells in both KO graft lines and of subsets of cone bipolar cells in *Isl1* KO ($Isl1^{-/-}$) retina grafts, both with enhanced host-graft synaptic formation, signal-to-noise ratio in RGC response, and improved light responsive behavior (Matsuyama et al., 2021). In the current study, in view of clinical application, we deleted the $ISL1^{-/-}$ gene to confirm the reproducibility of these features using hESC-retinas. We found a marked reduction in ON bipolar cells while sparing photoreceptors, Müller glia, and horizontal cells *in vitro* and/or *in vivo* after transplantation and a significant improvement in host RGC light responses in the transplanted retina with $ISL1^{-/-}$ hESC-retinas than with wild-type hESC-retinas using multiple electrode array system. We also identified expression of number of synaptic marker proteins at possible host-graft contact site. Furthermore, we analyzed the factors that may affect functional integration of the graft and found that a good host-graft contact as well as a good preservation of host inner retina may contribute to improved function of $ISL1^{-/-}$ hESC-retinas after transplantation.

RESULTS

Generation of an $ISL1^{-/-}$ retinal organoid from human ESCs

We obtained *ISL1* KO ($ISL1^{-/-}$) clones as summarized in Figures S1A–S1C using $Crx::Venus$ reporter hESC line (KhES-1), in which photoreceptor precursor cells and mature photoreceptors express Venus fluorescence (Nakano et al., 2012). $ISL1^{-/-}$ hESC clones were routinely maintained with the expression of PSC markers (Figure S1D). Retinal organoids were differentiated from $ISL1^{-/-}$ hESCs in a similar manner to wild-type (WT) hESCs, which were positive for a retinal progenitor cell (RPC) marker Chx10 at differentiation day (DD) 15 (Figures 1A, 1B, and S1E). The differentiated organoids of WT and $ISL1^{-/-}$ hESC showed the characteristic appearance of continuous neuroepithelium that expressed early born RGC marker Brn3 on the basal side at around DD60–90, whereas ISL1$^+$ cells were only present in the WT but not in the $ISL1^{-/-}$ hESC-retina (Figures 1C–1D and S1F–S1G). Consistently, the Crx$^-$/ISL1$^+$ population was absent in $ISL1^{-/-}$ hESC-retina at DD54 by flow cytometry (FCM) analysis (Figure 1E). Because photoreceptors are the essential part of an hESC-retina for transplantation, and RGCs are cells born earliest in the retina, we evaluated the differentiation of retinal organoids *in vitro* by characterizing their temporal and spatial distributions (Figure S2). Many Brn3$^+$ cells in WT hESC-retinas were also positive for ISL1, whereas ISL1$^+$ cells were absent in $ISL1^{-/-}$ hESC-retinas during differentiation culture. Interestingly, the number of Brn3$^+$ cells in $ISL1^{-/-}$ hESC-retinas was temporally approximated or was slightly higher than that in WT hESC-retinas, which eventually decreased to 5% in the organoids by DD110 (Figures 1F and S2). The differentiation of $Crx::Venus^+$ photoreceptors seemed roughly similar between the WT and $ISL1^{-/-}$ hESC-retinas (Figure 1G).

The proportions of the subtypes of retinal cells in the early stage of WT and $ISL1^{-/-}$ hESC-retinas (∼DD58) was similar, including Chx10$^+$/Crx$^-$ RPC (30%–40%), Pax6^{++} RGCs and amacrine cells (AC) (20%–30%), and
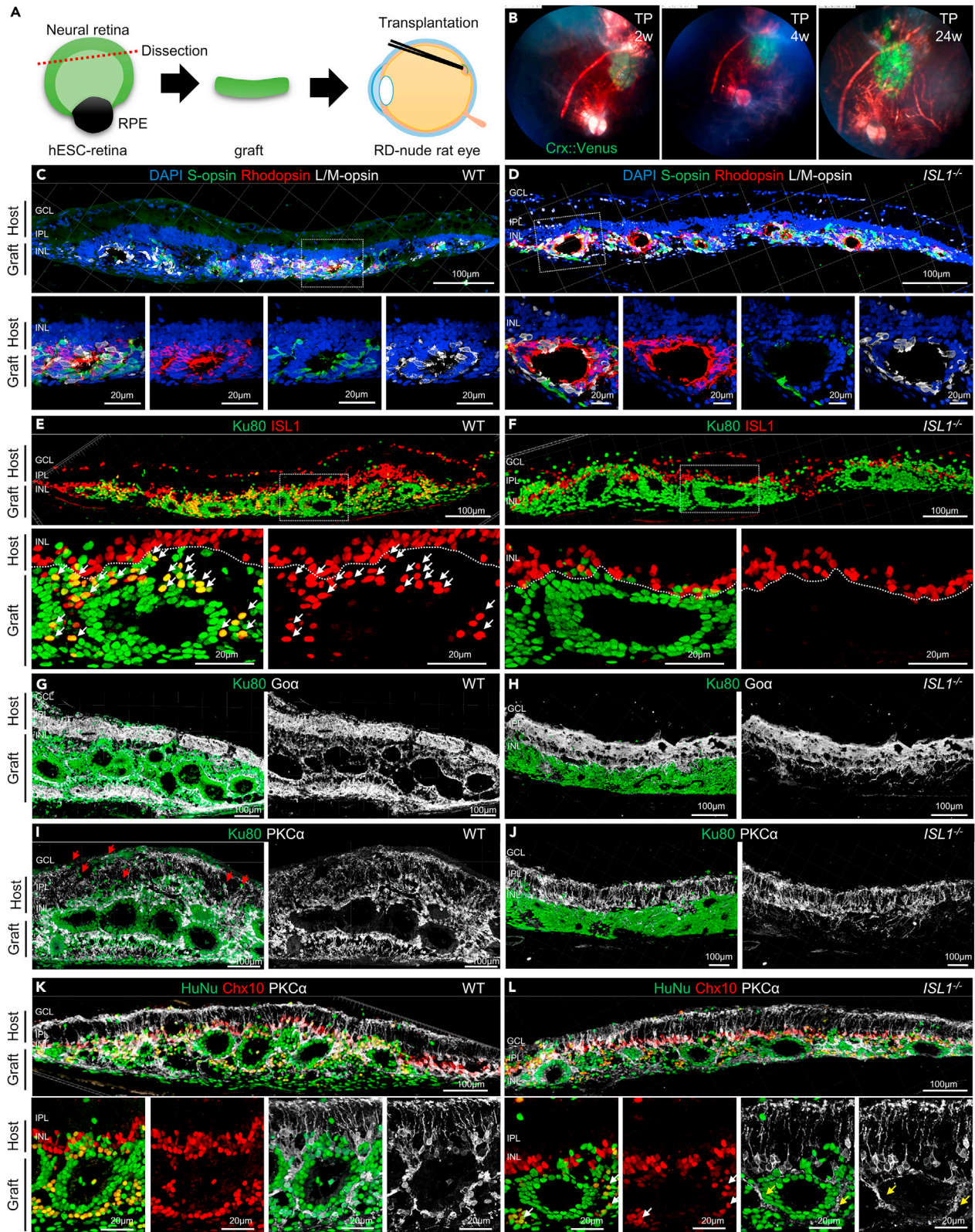
Figure 2. Maturation of hESC-retina after transplantation in RD-nude rats

(A) Schematic illustration of subretinal transplantation of hESC-retina.

(B) *In vivo* fundus imaging of transplanted *Crx::Venus*$^+$ hESC-retina on 2, 4, and 24 weeks after transplantation.

(C and D) Immunostaining for rat retina with S-opsin, L/M-opsin, and rhodopsin in WT and *ISL1*$^{-/-}$ hESC-retinas after 24 weeks of transplantation with DAPI nuclear staining.

(E and F) Ku80$^+$/ISL1$^+$ human inner cells (arrows) surround graft photoreceptors in the WT but were absent in *ISL1*$^{-/-}$ hESC-retina.

(G–J) Goα$^+$ or PKCα$^+$ ON/rod-bipolar cells were present in the Ku80$^+$ WT but not in *ISL1*$^{-/-}$ hESC-retina.

(K and L) Note that host bipolar dendrites were observed surrounding the graft photoreceptors (yellow arrows). A few Chx10$^+$/PKCα$^-$ cells were present in HuNu positive graft cells in *ISL1*$^{-/-}$ hESC-retina (white arrows). DD, differentiation day; TP, transplantation; GCL, ganglion cell layer; IPL, inner plexiform layer; INL, inner nuclear layer.

Crx::Venus$^+$ photoreceptors (10%–20%) that were mostly Rxrγ$^+$ cone photoreceptor precursor cells at this stage (Figures 1H and S3B); this indicates that deletion of the *ISL1* gene does not affect the differentiation of retinal cells including the photoreceptor precursor cells in the early stage. The RBPMS (pan-RGC) and Calretinin (subsets of RGC and AC) were also positive in the emerging inner layer where some cells were found positive for ISL1 in the WT hESC-retina (Figure S3C). We also checked the presence of ISL2 in WT and *ISL1*$^{-/-}$ hESC-retinas to find that ISL2$^+$ cells were decreased among RGC in *ISL1*$^{-/-}$ hESC-retina up to DD60 but were similarly observed among Rxrγ$^+$ cone photoreceptor precursor cells in both WT and *ISL1*$^{-/-}$ hESC-retinas at DD74 and after (Figure S3).

Loss of *ISL1* leads to drastic reduction of ON-bipolar cells in long-term *in vitro* culture

In order to observe the effect of *ISL1* deletion on late-born retinal cells such as photoreceptors and bipolar cells in human retinas, we observed WT and *ISL1*$^{-/-}$ hESC-retinas at around DD240. The appearances of WT and *ISL1*$^{-/-}$ hESC-retinas were similar, presenting fluffy cilium-like structures covering the apical surface (Figures 1I and 1S3D). *Crx::Venus*$^+$/Recoverin$^+$ photoreceptors were located in most apical and middle layers in both WT and *ISL1*$^{-/-}$ hESC-retinas (Figure 1J). The apically located photoreceptors developed inner-/outer-segment (IS/OS)-like structures expressing PRPH2 (Figures S4A–S4B). On FCM analysis, *Crx::Venus*$^+$ populations formed two groups based on Venus intensity (*Crx::Venus*$^+$ and $^{++}$), of which *Crx::Venus*$^{++}$ cells mostly expressed Recoverin and PRPH2 similarly in WT and *ISL1*$^{-/-}$ hESC-retinas (Figures 1K and S4A–S4B). These *Crx::Venus*$^{++}$ photoreceptors included cells positive for cone and rod photoreceptor markers S- and L/M-opsin, cone arrestin, and rhodopsin, and the majority of *Crx::Venus*$^{++}$ photoreceptors also expressed a synaptic marker PSD95 (Figure S4B). The characteristic localization of the cells positive for these markers was also confirmed by immunohistochemistry (IHC) (Figure S4A). The fraction of *Crx::Venus*$^{++}$ photoreceptors was about 40%, with a Nrl$^+$ rod to Rxrγ$^+$ cone photoreceptor ratio of about 1:1 (n = 4; >10 sheets for each) (Figures S4C–S4F). At around DD240, RPCs (Chx10$^+$/*Crx::Venus*$^-$, Chx10$^+$/Sox2$^+$, Pax6$^+$/Sox2$^+$) were identified in about 5% of the hESC-retinas but there were few Ki67$^+$ proliferating cells (Figures S4C–S4E).

As to bipolar cells, Goα$^+$ ON-bipolar cells, PKCα$^+$ or L7$^+$ rod bipolar cells were present in *Crx::Venus*$^+$ population by FCM and in the inner layer of the organoids in WT but absent or very infrequent in *ISL1*$^{-/-}$ hESC-retinas at DD240 (Figures 1M–1P and S4A–S4B). Secretagogin$^+$ cone bipolar cells were observed in both lines but as a very small population (Figures S4A–S4B). In spatial and temporal analyses, Goα$^+$ and PKCα$^+$ cells were observed from DD167 in WT hESC-retinas, which were also Chx10$^+$, suggesting that these are mature ON/rod-bipolar cells. We observed very few Goα$^+$ and PKCα$^+$ cells but a substantial number of Chx10$^+$ cells in *ISL1*$^{-/-}$ hESC-retinas (Figure S5A); these may include premature retinal cells or some Müller glia. Altogether, deletion of *ISL1* gene in hESC-retina reduced the number of ON/rod-bipolar cells without affecting the development of photoreceptors.

ISL1$^{-/-}$ hESC-derived retina survived and matured after transplantation into a rat model of retinal degeneration

Next, we transplanted retinal sheet into the subretinal space of a nude rat model of the end-stage retinal degeneration with few remaining photoreceptors, SD-Foxn1 Tg (S334ter) 3LavRrrc, at 16–25 postnatal weeks (Seiler et al., 2014; Tu et al., 2019). We dissected the *Crx::Venus*$^+$ retinal epithelium around DD60 to prepare a strip sheet of approximately 0.5 mm width for transplantation (Figure 2A and S5B). After transplantation, the graft formed multiple *Crx::Venus*$^+$ photoreceptor rosettes as observed by *in vivo* color fundus imaging (Figures 2B and S5C). At day 180 post-transplantation (i.e., ∼DD240), IHC image presented graft outer nuclear layer (ONL)-like structures expressing rhodopsin or S- and L/M-opsin in hESC-retinas of both WT and 2 *ISL1*$^{-/-}$ clones of 330A16 and 330A19 (Figures 2C–2D and S5G).
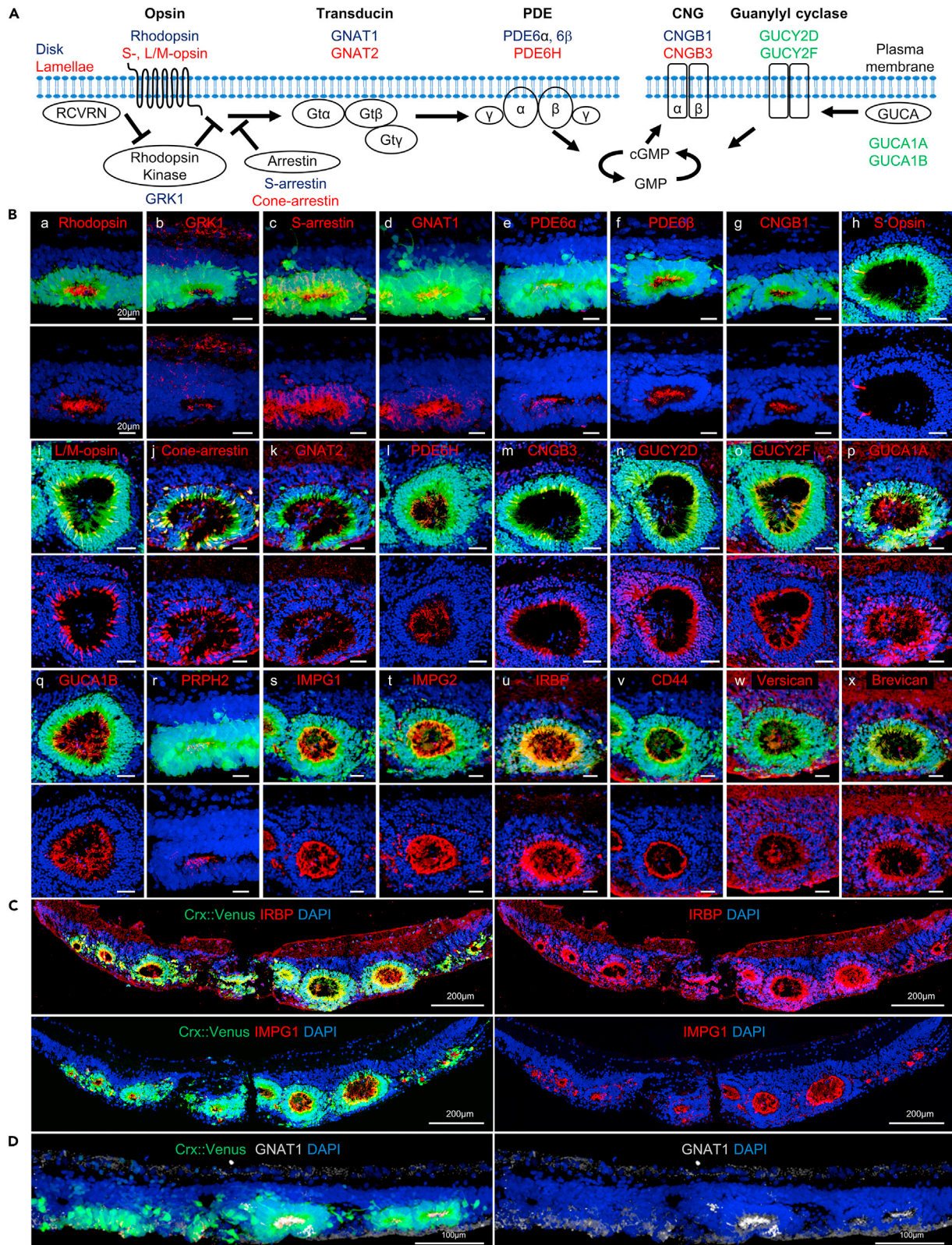
Figure 3. Expression of phototransduction protein and IPM protein in *ISL1*$^{-/-}$ hESC-derived photoreceptors after transplantation

(A) Summary of phototransduction signaling cascades.

(B) Expression of rod phototransduction proteins (a–g), cone phototransduction proteins (h–m), and guanylyl cyclase (GC) and GC-activating proteins (n–q) in the *Crx::Venus*$^+$ photoreceptor rosettes. Maturation of photoreceptors with IS/OS formation was indicated by PRPH2 (r). Expression of IPM proteins was found in the rosette (s–x).

(C and D) Expression of IRBP, IMPG1(C), and GNAT1 (D) in the *ISL1*$^{-/-}$ hESC graft.

The graft cells labelled by primate-specific nuclear marker Ku80 or HuNu were mostly confined to the graft area with some migration into the host retina (Figures 2E and 2F). In the WT hESC-retina grafts, many ISL1$^+$/Ku80$^+$ graft inner cells were observed between the host inner cells (ISL1$^+$/Ku80$^-$) and graft photoreceptors, whereas the direct contact between the host inner cells and graft photoreceptors was observed with the *ISL1*$^{-/-}$ hESC-retina grafts (Figures 2E, 2F, and S5H 330A19 line). These ISL1$^+$/Ku80$^+$ cells in the WT graft were mostly PKCα$^+$ rod bipolar cells (Figure S5D). The photoreceptor rosettes in the WT graft were densely surrounded by graft Goα$^+$ ON-bipolar or PKCα$^+$ rod bipolar cells, whereas those in the *ISL1*$^{-/-}$ hESC graft had no surrounding graft ON/rod-bipolar cells, which visualized host ON/rod-bipolar cells extending their dendrites into graft photoreceptors (Figures 2G–2J and S5–S5I'). Although HuNu$^+$/PKCα$^+$ cells were few, a very small number of HuNu$^+$/Chx10$^+$/PKCα$^-$ nonbipolar cells were still observed in *ISL1*$^{-/-}$ grafts (Figures 2K and 2L). Host bipolar cells often extended their long PKCα$^+$ dendrites to contact graft photoreceptors (Figures 2J and 2L).

Glutamate synthase (GS)$^+$ Müller glia and Calbindin$^+$ horizontal cells were similarly present in both WT and *ISL1*$^{-/-}$ grafts (Figures S5E–S5F). Interestingly, GS$^+$ Müller glia were observed stretching throughout the entire graft, whereas human GFAP was only positive in the graft near the host RPE, indicating the limited activation of graft Müller glia distal to the integration site. This was consistent with our previous observation (Tu et al., 2019; Yamasaki et al., 2021).

Collectively, *ISL1*$^{-/-}$ hESC-retina transplant presented reduced number of bipolar cells yet retaining the essential components such as photoreceptors, Müller glia, and horizontal cells in the organized structure with matured rod and cone photoreceptors.

Photoreceptors of the *ISL1*$^{-/-}$ hESC-retina mature functionally after transplantation

We then estimated photo-responsive potential of mature photoreceptors in *ISL1*$^{-/-}$ hESC-retinas after transplantation by confirming the presence of several key proteins that are involved in phototransduction signaling by IHC in PRPH2$^+$ mature graft photoreceptors (Figures 3A and 3B). In rat retinas six months after transplantation, graft photoreceptor rosettes formed the IS/OS-like structure in the internal space, which were positive for the rod phototransduction-pathway-related markers GRK1, S-arrestin, GNAT1, PDE6α/6β, and CNGB1 (Figures 3Ba–3Bg); the cone phototransduction-pathway-related markers cone arrestin GNAT2, PDE6H, and CNGB3 (Figures 3Bh–3Bm), and the rod and cone phototransduction pathway-related markers including GUCY2D, GUCY2F, GUCA1A, and GUCA1B (Figure 3Bn–3Bq).

In addition, we assessed the extracellular microenvironment in *ISL1*$^{-/-}$ hESC-retina after transplantation by immunostaining the interphotoreceptor matrix (IPM) components inside the rosette cavity. Interestingly, the internal space of graft photoreceptor rosettes, which was separate from the RPE, expressed IPM including IMPG1 (SPACR), IMPG2 (SPARCAN), IRBP, CD44, versican, and brevican, suggesting that these IPM were secreted by graft photoreceptors and/or Müller glia (Figure 3Bs–3Bx). IPM proteins were expressed in most of the photoreceptor rosettes; however, the phototransduction protein GNAT1 was typically observed in mature OS-like structures in relatively large rosettes (Figures 3C and 3D). All antibodies used here were checked using adult monkey retina (Figure S6A). These observations suggest that photoreceptors in transplanted *ISL1*$^{-/-}$ hESC-retinas not only express functional proteins but also may create a supportive environment for them to function.

Improved contact efficiency between host bipolar and graft photoreceptors in *ISL1*$^{-/-}$ hESC-retina

As the deletion of graft bipolar cells seemed to enhance host-graft contact, we evaluated host bipolar-graft photoreceptor contact by immunostaining Recoverin, PKCα, and Ku80 to classify the contact patterns into 3 types: *Poor*, graft bipolar cells are present between host bipolar cells and graft photoreceptor rosettes, with no apparent host-graft contact. *Fair*, some host bipolar cells reach toward graft photoreceptors,
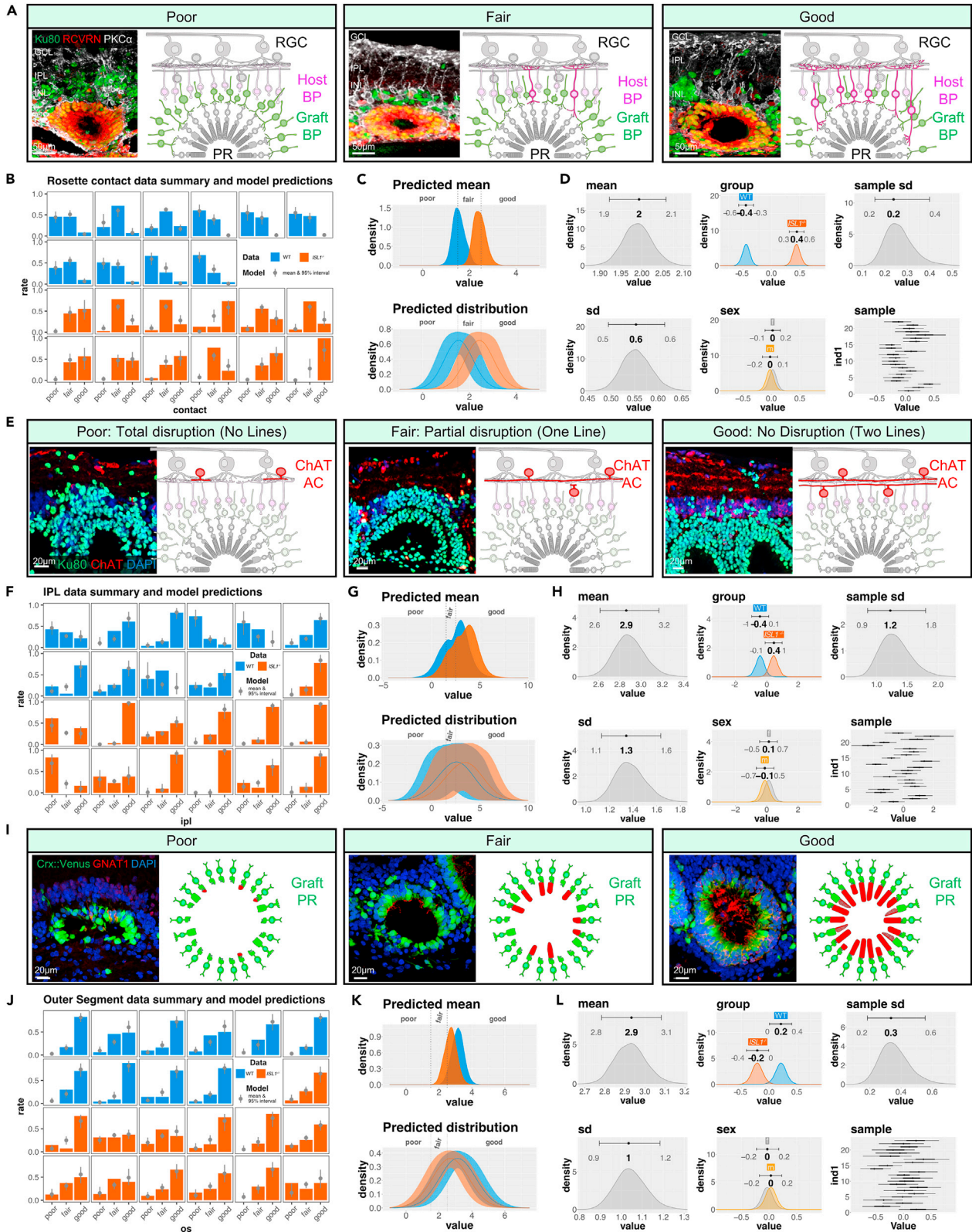
Figure 4. Histological pattern comparison between the WT and *ISL1*$^{-/-}$ retina grafts

(A, E, and I) Schematic representations of three patterns: *poor*, *fair*, and *good* for rosette contact. (A) IPL preservation (E) and OS elongation (I).

(B, F, and J) Summary of data (bars) indicating the rate of *poor*, *fair*, and *good* per sample (transplanted retina), along with model predictions (dot and bars indicating mode and 95% compatibility interval) for rosette contact (B), IPL preservation (F), and OS elongation (J).

(C, G, and K) Distributions of predicted mean (top: predicted mean) and expected distribution (bottom: predicted distribution) for rosette contact. (C) IPL preservation (G) and OS elongation (K).

(D, H, and L) Posterior distribution of model parameters: rosette contact. (D) IPL preservation (H) and OS elongation (L). Bars above graphs indicate mode and 95% compatibility interval. A total of 541 rosettes (311 WT and 230 *ISL1*$^{-/-}$ rosettes, from 10 WT to 12 *ISL1*$^{-/-}$ transplanted retinas) were used for rosette contact analysis, 493 IPL areas under rosettes (222 WT and 271 *ISL1*$^{-/-}$ areas under rosettes, from 10 WT and 13 *ISL1*$^{-/-}$ hESC-retinas) were used for the IPL analysis, and 614 rosettes (298 WT and 316 *ISL1*$^{-/-}$ rosettes, from 10 WT and 13 *ISL1*$^{-/-}$ hESC-retinas) were used for the OS analysis. BP, bipolar cells; PR, photoreceptors; AC, Amacrine cells.

although graft bipolar cells are present between graft photoreceptors and host bipolar cells. *Good*, most graft photoreceptors are bordering host bipolar cells (Figure 4A) The quantitative data, as the rate of observed contact type (*poor*, *fair*, *good*) by sample, demonstrated about half the rosettes in WT hESC-retinas had poor contact, whereas *good* contact was observed in about half of the rosettes in *ISL1*$^{-/-}$ hESC-retinas (Figure 4B). We modeled these ordinal data (*poor* < *fair* < *good*) assuming an underlying metric variable with a normal distribution with cutoff thresholds for *poor* = 0.5 and *good* = 2.5 and estimated its mean and standard deviation considering graft group (WT or *ISL1*$^{-/-}$), host sex, and sample bias using hierarchical Bayesian modeling (Figure 4B). The distributions of predicted mean for WT and *ISL1*$^{-/-}$ and the distribution of predicted values, i.e. the expected distribution when taking into account the standard deviation (sd), were calculated (Figure 4C). The rosette contact data had an overall mean of approximately 2 with sd 0.6. There was a clear and substantial effect of the group (difference of WT and *ISL1*$^{-/-}$ is −0.9 [95% interval: −1.2 to −0.6]), strongly indicating that *ISL1*$^{-/-}$ hESC-retinas had better contact compared with WT hESC-retinas (Figure 4D). Host sex did not influence rosette contact, and sample bias was relatively small (sample sd is about 0.2).

The *ISL1*$^{-/-}$ hESC-retina better preserved the host IPL structure but may have fewer rod outer segments than WT

Although we have not observed any undesirable proliferation of graft retinas after transplantation, grafted retinal cells sometimes migrated into host retinas, causing varying degrees of disorganization of the structure of the host retina (Figure 2I, red arrow). Thus, we evaluated the degree of host IPL disorganization in areas adjacent to photoreceptor rosettes. We stained choline acetyltransferase (ChAT) and categorized the IPL state into *poor*, *fair*, or *good* based on the pattern of the two IPL lines that were usually present (Figure 4E): *Poor*, both IPL lines were disrupted. *Fair*, one of the IPL lines was disrupted. *Good*, both IPL lines were preserved. The summary of collected data alongside model predictions, as the proportion of observed IPL pattern (*poor*, *fair*, *good*) by sample, are shown with modeling analysis (Figures 4F–4H). IPL preservation data have an overall mean of approximately 2.9 sd 1.3 with a small effect of group (Figure 4H group, difference of WT and *ISL1*$^{-/-}$ hESC-retina is −0.9 [95% interval: −1.9 to 0.2]). Overall, host retinas transplanted with *ISL1*$^{-/-}$ hESC-retinas seemed to have less disrupted IPL structure but the difference was not immediately apparent in samples due to both the large sd of the distribution and large sample biases.

We also evaluated IS/OS growth by the staining patterns of the phototransduction protein GNAT1 in graft photoreceptors. The growth of OS expressing GNAT1 was graded into three patterns (Figure 4I): *Poor*, unclear polarization of GNAT1 and no apparent IS/OS structures; *Fair*, sparse presence of polarized GNAT1 positive IS or OS; *Good*, GNAT1 positive OS within the central space of the rosette. A summary of collected data alongside model predictions and modeling analysis is presented in Figures 4J–4L; OS growth data have an overall mean of approximately 2.9 with sd 1. There is a small but credible effect of group (Figure 4L group; difference between WT and *ISL1*$^{-/-}$ hESC-retina is 0.4 [95% interval: 0.0 to 0.8]); this indicates that, although OS growth was mostly good in both groups, retinas transplanted with *ISL1*$^{-/-}$ hESC-retinas seemed to have shorter/fewer IS/OS structures although the effect was subtle.

Presence of multiple synaptic components suggested a formation of host-graft synapses after transplantation of *ISL1*$^{-/-}$ hESC-retina

With the *ISL1*$^{-/-}$ hESC-retina graft, in the absence of graft rod bipolar cells, we could clearly identify PKCα$^+$ host rod bipolar dendrites reaching toward the photoreceptors, which allowed us to confirm multiple synaptic components at host-graft synapses. *Crx::Venus*$^+$-grafted photoreceptors expressed ribbon synapse
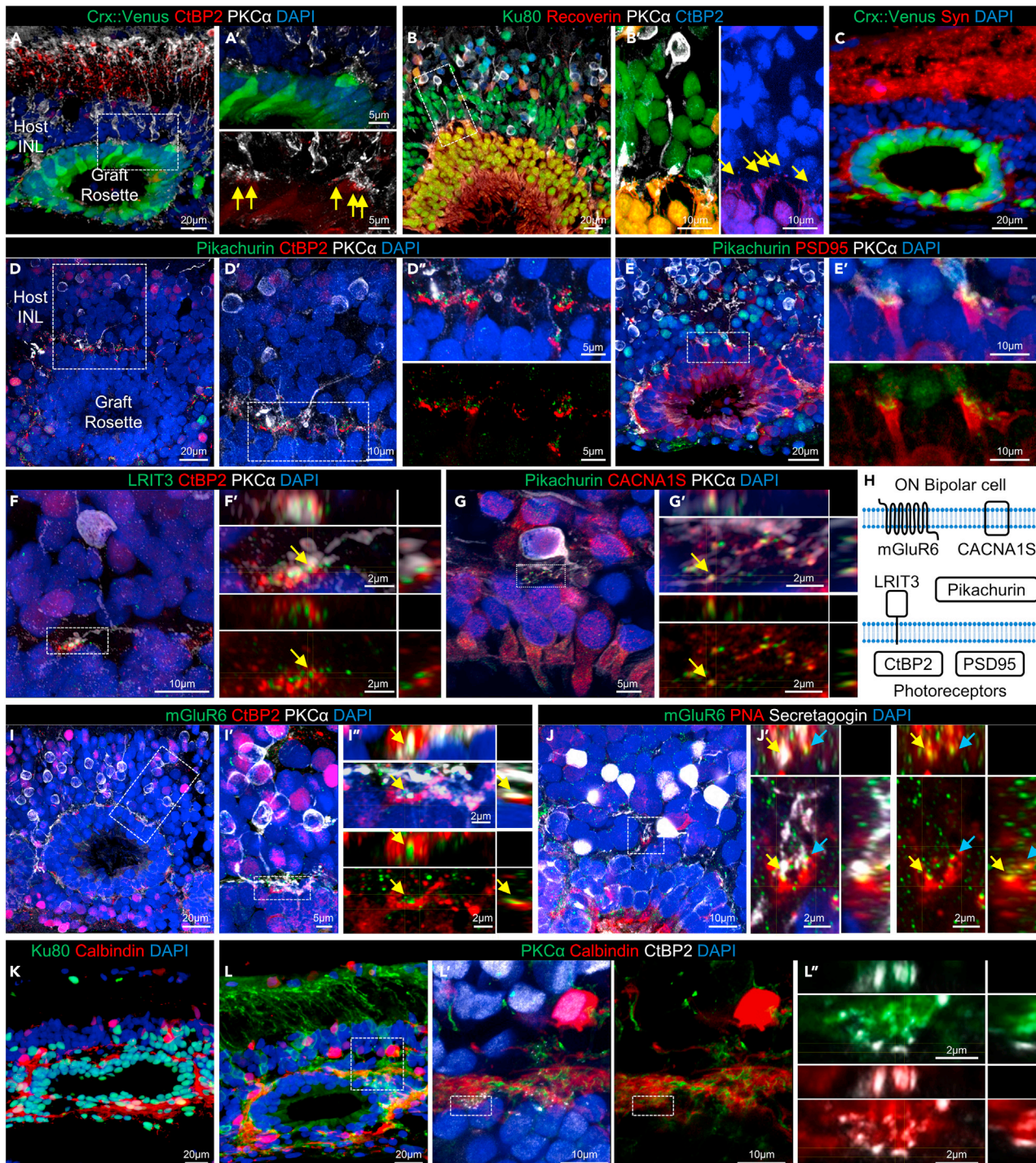
Figure 5. Host-graft synaptic formation of transplanted photoreceptors derived from *ISL1*$^{-/-}$ hESC-retina

(A and B) Presynaptic marker CtBP2 was localized on the margin of the *Crx*::Venus$^+$/Recoverin$^+$ photoreceptors and the dendritic tips of Ku80$^-$/PKCα$^+$ host bipolar cells (yellow arrows).

(C) Outer Plexiform layer-like structures formed with synaptophysin (Syn) around the rosette.

(D–F) Presynaptic proteins pikachurin, CtBP2, PSD95, and LRIT3 were present at the dendritic tips of PKCα$^+$ host rod bipolar cells. (G) Postsynaptic marker CACNA1S were coupled with pikachurin.

Figure 5. Continued

(H) Schematic illustration showing the major elements in the photoreceptor-ON-bipolar synapses.

(I) Putative CtBP2/mGluR6 synaptic complexes were present at the extended dendritic tips of PKCα[+] host rod bipolar cells.

(J) Putative PNA/mGluR6 cone photoreceptor synapse formation was observed at the dendrite tips of Secretagogin[+] cone bipolar cells.

(K–L) Host (Ku80^{−}) and graft (Ku80^{+}) Calbindin^{+} horizontal cells dendrites were observed surrounding graft rosette.

marker CtBP2 at the tips of host bipolar dendrites (Figure 5A) (Matthews and Fuchs, 2010; Tom Dieck et al., 2005). Host rod bipolar cells often extended dendrites even through the occasionally present graft inner cells (Ku80^{+}/Recoverin[−]) to reach graft photoreceptors (Figure 5B). Transplanted photoreceptors also exhibited synaptophysin, the synaptic vesicle protein, around ONL-like rosette structures, suggesting the synaptic maturation of graft photoreceptors (Figure 5C). Another synaptic protein pikachurin, which contributes to precise synaptic interaction as a dystroglycan ligand, was found to localize in the cleft of CtBP2-labeled, horseshoe-shaped synaptic ribbons around the graft rosette at the tips of PKCα[+] dendrites (Figure 5D) (Sato et al., 2008). Presynaptic protein PSD95 also colocalized with pikachurin at the photoreceptor terminals (Figure 5E). LRIT3, a synapse protein involved in coordination of the transsynaptic communication between the rod and rod bipolar cells (Hasan et al., 2019), was observed with CtBP2 at the dendrite tips of a host rod bipolar cell (Figure 5F). We further observed postsynaptic proteins CACNA1S and mGluR6 on the host bipolar dendrite tips (PKCα or cone bipolar Secretagogin) coupled with pikachurin, CtBP2, and PNA (cone pedicle marker) to form putative rod and cone synaptic complexes at the margin of graft photoreceptor rosettes (Figures 5G–5J). High-magnification images show that mGluR6 puncta were located adjacent to CtBP2 and peanut agglutinin (PNA), suggesting the presence of host-graft synaptic complexes (Figure 5I'' and 5J'). Finally, we determined whether horizontal cells, a component of the typical triad photoreceptor synapse, are involved in the formation of host-graft photoreceptor synapses. Calbindin[+]/Ku80^{+} graft horizontal cells were present in the *ISL1*^{−/−} hESC-retina, and Calbindin[+] axons or dendrites either from host (Ku80^{−}) or graft (Ku80^{+}) horizontal cells surround the graft rosette (Figure 5K). We observed a possible synaptic assembly of PKCα[+] host bipolar cell, Calbindin[+] horizontal cell dendrites, and CtBP2^{+} graft photoreceptor terminals (Figure 5L). All the synaptic antibodies used here were checked in adult nude rat retina (Figure S6B). These data suggest that photoreceptors in *ISL1*^{−/−} hESC-retinas are highly capable of forming functional synapses with host bipolar cells.

ISL1^{−/−} hESC-retinas elicited better light responses in host RGCs than WT hESC-retinas

Multi-electrode array (MEA) recordings of the transplanted rat retinas were conducted at 60 weeks old or later (8–10 months after transplantation), where almost no RGC light responses were observed with the scotopic-mesopic light stimuli (10.56 log photons/cm^2/s, referred to as *weak* stimuli hereafter) (Tu et al., 2019). To assess the light responses derived from the transplanted hESC-retinas, the freshly isolated retina was mounted with the grafted area centered at the MEA electrodes and the optic nerve disc within sight, as in the example shown in Figure 6A. The *Crx::*Venus[+] rosettes of WT or *ISL1*^{−/−} hESC graft were confirmed to have bright green fluorescence after recordings (Figure 6B). The peri-stimulus time histograms (Figure 6C) and raster plots (Figure 6D) of this sample suggest the host RGC light responses were spatially correlated with the graft coverage, consistent with other transplanted retinas of both WT and *ISL1*^{−/−} hESC graft. For most transplants, retinas from the opposite, nontransplanted eyes were used as the age-matched control. Presence of light responses sensitive to the mGluR6 blocker L-AP4 in transplanted retinas implied functional synaptic transmissions between photoreceptors and bipolar cells (Figure 6E), In contrast, relatively few light responses were detected in control retinas, mostly with strong (12.84 log photons/cm^2/s) and super-strong (15.48 log photons/cm^2/s) stimuli, which possibly originated from residual cone photoreceptors, if any, or melanopsin-expressing RGCs that were not sensitive to L-AP4 blockade. Note that the super-strong stimuli were only applied at the end of experiments for all samples to confirm their viability.

The population averages of RGC spiking frequency revealed a higher baseline firing rate in control retinas (Figure 6E), especially in the presence of L-AP4. Figure 6G shows the distribution of averaged spontaneous firing rate (spontaneous spiking before light stimulation). The spontaneous activity has a lognormal distribution, as we have reported previously (Matsuyama et al., 2021). We estimated the effect of different parameters (group, sex, L-AP4 treatment, stimulus strength, and sample bias) on the spontaneous activity using hierarchical Bayesian inference. The overall mean (log) of the firing frequency distribution was 1.68 (95% interval: 1.66 to 1.70), which is equivalent to 5.4 Hz, with sd 1.02 (95% interval: 1.01 to 1.02). The mean is indicated in Figure 6G by the vertical line. The *group* has a clear effect on spontaneous spiking (Figure 6H group), with transplanted retinas showing less spontaneous firing (difference of control and WT is 0.7 [95% interval: 0.4 to 0.9] and control and *ISL1*^{−/−} is 0.5 [95% interval: 0.3 to 0.8]). There was no effect of
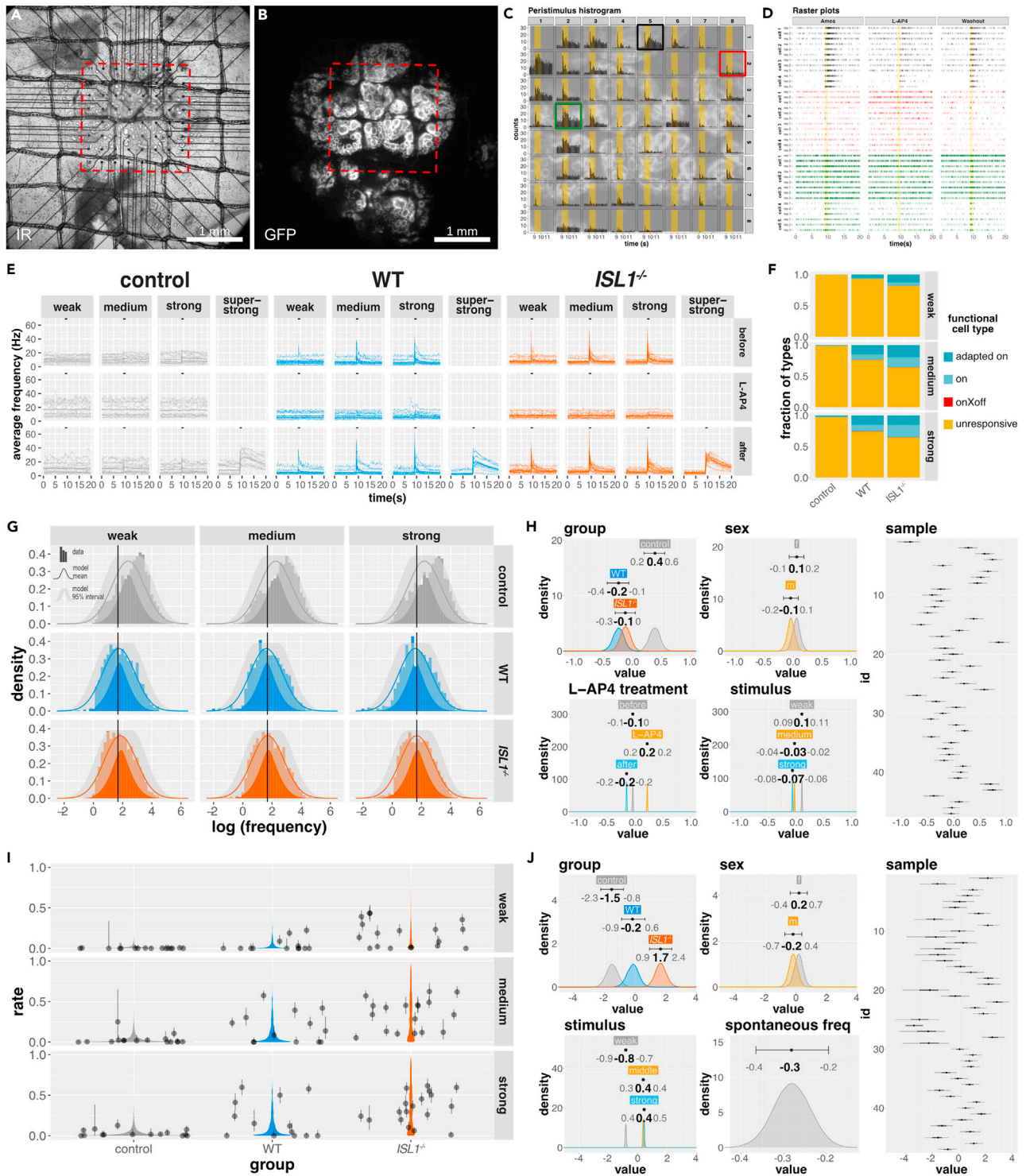
Figure 6. Light responses of transplanted retina by MEA recordings

(A–D) Representative recordings of transplanted ($ISL1^{-/-}$) hESC-retina using MEA system. Transplanted rat retina (A) was mounted on the MEA probe with the Crx::Venus⁺ hESC-retina centered on electrode area (B) indicated by red boxes. (C) Peri-stimulus time histogram of host RGC spikes with responses to strong light stimuli after washout of L-AP4. Detailed raster plots from three channels (highlighted in black, red, and green) are shown in (D).

Figure 6. Continued

(E) Population averages of transplanted retinas with WT and $ISL1^{-/-}$ hESC-retinas and nontransplanted control retinas. Thin lines represent the sample average and thicker lines represent the group averages for the respective L-AP4 treatment condition (before, L-AP4, after) and light stimulation (weak, medium, strong, super-strong).

(F) Breakdown of the functional RGC types detected in both transplanted and control retinas.

(G) Distribution of RGC spontaneous firing (log(Hz)). Vertical lines indicate the estimated overall mean (1.68). Bars summarize recorded data, whereas lines and ribbon plots show the mode and 95% compatibility interval of model posterior predictions.

(H) Posterior distribution of model parameters for RGC spontaneous activity.

(I) Summary of RGC response probability with light stimulation. Dots and bars show per sample summary of collected data with lines showing the Clopper and Pearson binomial 95% confidence interval. Violin plots show the model posterior predictions.

(J) Posterior distribution of model parameters for RGC responsiveness. Note that values represent log odds. These data in this figure was collected from a total of 47 retinas (16 control, 13 WT, and 18 $ISL1^{-/-}$ graft transplanted retinas).

host *sex* (Figure 6H sex). Similar to our previous finding in mice (Matsuyama et al., 2021), there was a small but distinct effect of *stimulus strength*, with spontaneous activities increased after brighter stimulation (Figure 6H stimulus). We also found that spontaneous activity clearly increased upon L-AP4 blockade (Figure 6H L-AP4 treatment). Finally, there was a relatively large effect of *sample* (Figure 6H sample, sample sd estimated to be 0.4 [95% interval: 0.3 to 0.5]).

To better characterize and compare the light responsiveness in transplanted retinas with robust RGC spontaneous firing, we classified the detected host RGCs, in consideration of their sensitivity to L-AP4 blockade and recovery after L-AP4 washout, into *unresponsive*, *onXoff*, *on*, and *adapted on* types (Figure 6F; see STAR Methods for further details) (Matsuyama et al., 2021). Most of the responding cells in transplanted retinas were *on* or *adapted on* types with similar *on* to *adapted on* ratios in both types of transplanted retinas. Figure 6I summarizes cell response rate (i.e., the probability that each detected cell would not be *unresponsive*) per sample upon different levels of light stimulation. We modeled the response probability using logistic regression that took into consideration of the group, sex, stimulus, and sample bias as predictors. The overall mean (log odds) was −3.2 (95% interval: −3.4 to −3.0). Figure 6J shows the posterior estimates of parameters. There was a clear and substantial effect of *group* (Figure 6J group, control < WT < KO ($ISL1^{-/-}$), difference of control and WT is −1.4 (95% interval −2.6 to 0), control and KO ($ISL1^{-/-}$) is −3.2 (95% interval −4.4 to −1.9), and WT and KO ($ISL1^{-/-}$) is −1.7 (95% Interval −3.1 to −0.6). There was no appreciable effect of host *sex* (Figure 6J sex). Light responses were clearly increased in *medium* (12.16 log photons/cm^2/s) and *strong* light stimulation compared with *weak* stimulation (Figure 6J stimulus, difference of weak and medium was −1.2 [95% interval −1.3 to −1.1], weak– and strong was −1.2 [95% interval −1.4 to −1.1]). *Sample* bias was substantial, with sample sd estimated to be 1.7 (95% interval 1.3–2.2) (Figure 6J sample). In addition to the above predictors, we used the average spontaneous firing rate during L-AP4 treatment as a covariate and found that it was inversely correlated with light responsiveness (Figure 6J spontaneous freq).

Light responsiveness after transplantation positively correlated with host-graft contact rate and well-preserved host IPL

So far, we have observed some differences in our immunohistological characterization (rosette contact, IPL preservation, and IS/OS growth) and in light responsiveness by electrophysiology, and it was therefore intriguing to elucidate which are the important factors that affect the functional output after transplantation. For this purpose, we further estimated correlation coefficients (ρ) among the different features, using the sample estimates from the respective analyses: light response probability for light responsiveness, mean (log) of the spontaneous firing for the analysis of spontaneous activity, and the mean of the underlaying metric variable for rosette contact, OS growth, and IPL preservation analyzes. We used the Student's t-distribution for the bivariate distribution, as the number of available samples was relatively small (21 samples). The number of estimated degrees of freedom for the Student's t-distribution was 18.8 (95% interval: 5.8–46.5). Pair plots in Figure 7 shows a summary of the relationships between features (lower) and estimated correlation coefficients (upper). Spontaneous activity did not seem to be correlated with any feature. On the other hand, rosette contact (ρ =0.4 [95% interval 0.0 to 0.7]), OS growth (ρ =-0.5 [95% interval −0.7 to −0.1]), and IPL preservation (ρ =0.5 [95% interval 0.1 to 0.7]) were weakly to moderately correlated to light responsiveness. Note that contact and IPL were positively correlated, whereas OS growth was negatively correlated. Rosette contact was positively correlated to IPL (ρ =0.4 [95% interval 0.0 to 0.7]) and negatively correlated to OS elongation (ρ =-0.4 [95% interval −0.7 to −0.1]). Finally, there was a potential weak negative correlation between IPL preservation and OS growth (ρ =-0.2 [95% interval −0.5 to 0.2]). Overall, the

A

B

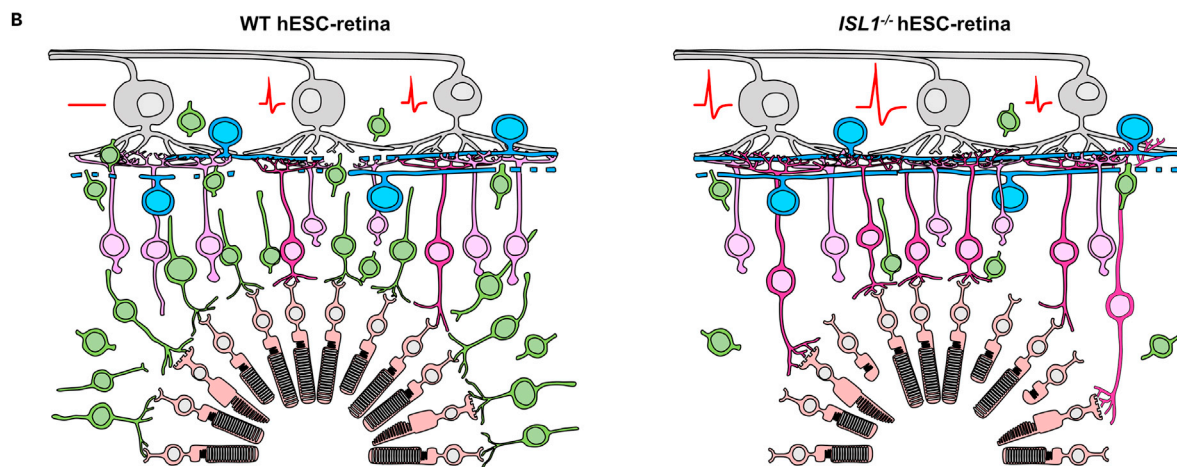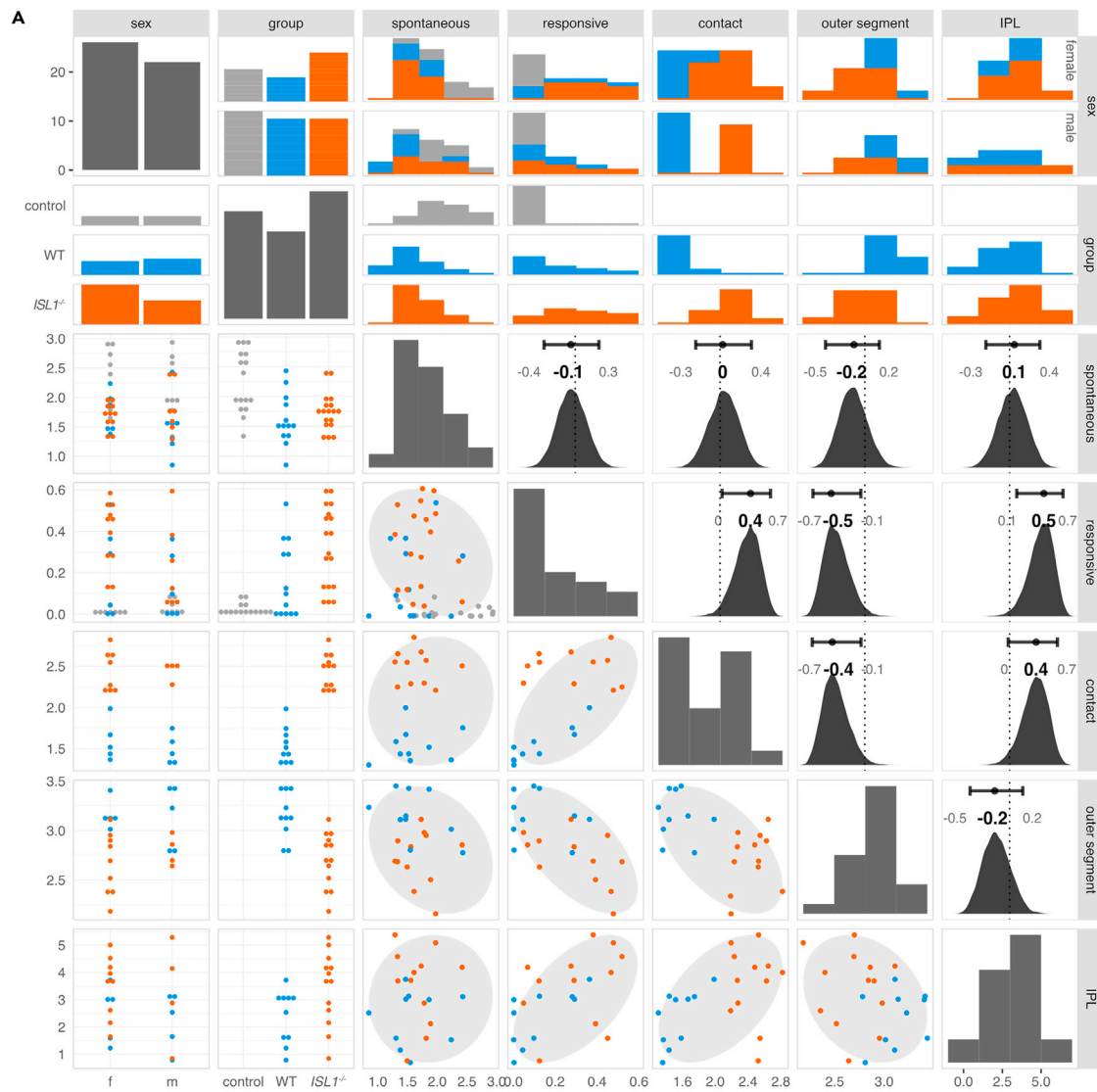WT hESC-retina   *ISL1*^{-/-} hESC-retina

Figure 7. Factors affecting light responsiveness after transplantation

(A) Pair plot of light responsiveness, spontaneous activity, rosette contact, IPL preservation, and OS elongation. Per sample predictions from the respective analyses were used to analyze correlation between these five features: responsive (estimated light response probability); spontaneous (estimated mean (log) spontaneous firing frequency); contact, OS, and IPL (the estimated mean of the underlying metric variable for the ordinal probit regression, with higher values indicating better performance). In addition to the features mentioned earlier, sex (female or male) and group (control, WT, and $ISL1^{-/-}$) breakdowns are also shown. The diagonal shows the distribution of values (histograms for continuous variables and bar chart for categorical variables). The plots below the diagonal show scatterplots, and the upper triangular plots show the posterior estimates of correlation coefficients with mode and 95% interval indicated on top or the per category breakdown of the distribution for categorical variables. Control samples are shown in gray, WT in blue, and $ISL1^{-/-}$ in orange.

(B) Schematic illustration of a summary of our results. $ISL1^{-/-}$ hESC-retina (right) has reduced graft bipolar cells, a greater number of host-graft cell contact, and better RGC light responses compared with WT hESC-retina (left) after transplantation.

data suggest that better rosette contact, IPL preservation, and light responsiveness were positively correlated to each other, whereas OS growth was negatively correlated to these.

DISCUSSION

Our work demonstrated proof-of-concept regarding the therapeutic approach using combination of gene engineering and regenerative medicine for retinal degeneration, i.e., the deletion of a key cell fate regulator gene to achieve an ideal type of retinal graft consisting mostly of essential cell types in a structured form upon maturation after transplantation. The deletion of $ISL1^{-/-}$ gene in hESC retinas resulted in a reduced number of ON-bipolar cells, the second neurons that receive signals from photoreceptors, sparing the subsequent photoreceptor cells, Müller glia, horizontal cells, and facilitated functional host-graft integration after transplantation; this was consistent with our previous observation using genetically engineered mouse ESC/iPSC retina grafts with the deletion of *Isl1* or *Bhlhb4* gene (Matsuyama et al., 2021). In this study, we further accessed detailed phenotypes of *ISL1* gene deletion in hESC-retina to pursue possible benefits in view of future clinical application. Mature graft photoreceptors in an organized layer expressed phototransduction cascade proteins after transplantation, assuring the function of these grafts as photoresponsive transplants. These $ISL1^{-/-}$ hESC-retinas resulted in increased host-graft contact with improved light responsiveness in the host RGCs compared with the WT hESC-retinas. Moreover, the host-graft synapse formation was confirmed by the presence of multiple synaptic markers using IHC even under a xenotransplantation condition.

It is noteworthy that graft photoreceptors in rosettes may create a microenvironment similar to that of interphotoreceptor space in normal retina, by expressing several IPM proteins within the rosette cavity even when kept distant from the RPE. The retinoid transporter IRBP, known to transport all-*trans*-retinal and 11-*cis* retinal for visual pigment recovery, was strongly expressed inside the rosette structures (Palczewski et al., 1999). It is unclear if the amount of 11-*cis* retinal delivered inside the rosettes is enough for retinoid cycles, but our MEA data at least showed that transplanted retinas were able to respond to light repetitively after isolation from RPE, without rod/cone opsin recovery by the addition of 9-*cis* retinal, suggesting some compensation may exist in the graft rosette environment. Interestingly, some rosettes exhibited ONL-like structures with a thinner photoreceptor layer on the RPE side, mimicking the correct orientation of ONL (Figure 2L). We previously reported that most of the rosettes that remained 2 years after xenotransplantation in the monkey model had a hemispherical shape with the opening facing the host RPE, potentially allowing retinoic acid cycling to happen (Tu et al., 2019). We also observed here and previously that the expression of GFAP or HLA class I was only enhanced on the RPE side of graft rosettes that failed to integrate with the host retina, indicating that nonintegrated photoreceptors were relatively prone to degenerate after transplantation (Yamasaki et al., 2021).

Lastly and most importantly, our MEA analysis together with the immunohistochemical analysis suggest the presence of essential factors for graft-driven retinal reconstruction. As we initially expected, the restoration of light responsiveness correlated positively with the host-graft contact rate that potentially resulted from the reduction of graft inner cells in $ISL1^{-/-}$ hESC-retinas, which, surprisingly and beneficially, correlated to better-preserved host IPL organization. In contrast, the thick layers of graft retinal inner cells that were sometimes observed on the RPE side in WT hESC-retinas may hinder visual pigment recycling via RPE in graft photoreceptors. These findings possibly explain the better anatomical and functional reconstruction of rat retinas transplanted with $ISL1^{-/-}$ hESC-retina compared with those seen with WT hESC-retina. However, WT hESC-retina was better than $ISL1^{-/-}$ hESC-retina in terms of their GNAT1$^+$ IS/OS morphology. We previously reported that thinning of the graft photoreceptor layer (ONL) by transplantation of the graft at later days of differentiation possibly resulted from a subsequent reduction in graft inner cells, implying a supportive role of inner cells for photoreceptor

survival and maturation. We therefore suggested that there was a necessary trade-off between ONL thickness and host-graft direct contact (Shirai et al., 2016). Here again, the negative correlation between the IS/OS status and RGC responsiveness may imply this trade-off. However, better performance by $ISL1^{-/-}$ hESC-retinas may imply that these transplanted retinas already have an excess functional photoreceptors compared with host-graft synapse formation and that currently host-graft contact and host IPL preservation are the most critical requirements for functional graft integration.

In the current study, the retinal cell profiles were not much different between the WT and $ISL1^{-/-}$ hESC-retinas at the time of transplantation but resulted in different phenotypes after transplantation. A beneficial tip of gene engineering may lie in the case of progenitor cell transplantation as seen in our case, where the graft progenitor cells at the time of transplantation further differentiate and mature, when the engineered gene plays a role to realize the pre-set phenotype sometime after transplantation. By this approach, we were also able to retain the organized structure of the retina transplants, which would be difficult to achieve by purification of graft cells before transplantation. Hence, our approach here would provide a new conceptual approach for utilizing gene engineering in regenerative medicine.

Limitations of the study

Since the report on material transfer from graft photoreceptors to remaining host photoreceptors, whether the reconstructed RGC responses are genuinely derived from the graft photoreceptors or from the rescued host photoreceptors has been a matter of concern (Pearson et al., 2016; Santos-Ferreira et al., 2016; Singh et al., 2016). We believe that immunostaining of multiple synapse markers at host-graft cell contact site are highly suggestive of the presence of some host-graft synaptic connections, but the evidence to directly show how much of these synapses contribute to what part of signaling output by host RGC is yet technically challenging. Other approaches including 3-dimentional electron microscopy or possibly some visual tracing of neuronal-cell activity transmission, for example, may provide further evidence. At present, however, we believe that evident improvement of physiological contact between host bipolar and graft photoreceptor cells associated with a substantial improvement of RGC light responses provides a promising possibility for retinal network reconstruction by cell therapies.

STAR★METHODS

Detailed methods are provided in the online version of this paper and include the following:

- KEY RESOURCES TABLE
- RESOURCE AVAILABILITY
  - ○ Lead contact
  - ○ Materials availability
  - ○ Data and code availability
- EXPERIMENTAL MODEL AND SUBJECT DETAILS
  - ○ Human ES cell line
  - ○ Rat model
- METHOD DETAILS
  - ○ Establishment of $ISL1^{-/-}$ hESC line
  - ○ Retinal differentiation and long-term culture
  - ○ Flow cytometry
  - ○ Transplantation into retinal degeneration model nude rats
  - ○ Multi-electrode array (MEA) recording
  - ○ Immunohistochemistry (IHC)
  - ○ Quantification analysis
  - ○ Statistical analysis

SUPPLEMENTAL INFORMATION

Supplemental information can be found online at https://doi.org/10.1016/j.isci.2021.103657.

AUTHOR CONTRIBUTIONS

M. M. and M.T. designed and supervised the study. S. Y. and T. H. generated the $ISL1^{-/-}$ hESCs. S. Y. and M. H. conducted FCM and IHC analysis. M. M. and J. S. conducted transplantation surgeries. S. Y. and T. M. conducted quantitative analysis. A. Ku., S.Y., A. Ki., and T. K. developed the protocol for 3D retinal differentiation culture from feeder-free hPSCs. H-Y. T. and T. M. conducted MEA recording and data analysis. S. Y., H-Y. T., T. M., and M. M. wrote the manuscript. All authors reviewed and approved the final manuscript.

DECLARATION OF INTERESTS

REFERENCES

Assawachananont, J., Mandai, M., Okamoto, S., Yamada, C., Eiraku, M., Yonemura, S., Sasai, Y., and Takahashi, M. (2014). Transplantation of embryonic and induced pluripotent stem cell-derived 3D retinal sheets into retinal degenerative mice. Stem Cell Rep. 2, 662–674.

Bramblett, D.E., Pennesi, M.E., Wu, S.M., and Tsai, M.J. (2004). The transcription factor Bhlhb4 is required for rod bipolar cell maturation. Neuron 43, 779–793.

Bringmann, A., Pannicke, T., Biedermann, B., Francke, M., Iandiev, I., Grosche, J., Wiedemann, P., Albrecht, J., and Reichenbach, A. (2009). Role of retinal glial cells in neurotransmitter uptake and metabolism. Neurochem. Int. 54, 143–160.

Eiraku, M., Takata, N., Ishibashi, H., Kawada, M., Sakakura, E., Okuda, S., Sekiguchi, K., Adachi, T., and Sasai, Y. (2011). Self-organizing optic-cup morphogenesis in three-dimensional culture. Nature 472, 51–58.

Elshatory, Y., Everhart, D., Deng, M., Xie, X., Barlow, R.B., and Gan, L. (2007). Islet-1 controls the differentiation of retinal bipolar and cholinergic amacrine cells. J. Neurosci. 27, 12707–12720.

Hasan, N., Pangeni, G., Cobb, C.A., Ray, T.A., Nettesheim, E.R., Ertel, K.J., Lipinski, D.M., McCall, M.A., and Gregg, R.G. (2019). Presynaptic expression of LRIT3 transsynaptically organizes the postsynaptic glutamate signaling complex containing TRPM1. Cell Rep 27, 3107–3116.e3.

Iraha, S., Tu, H.Y., Yamasaki, S., Kagawa, T., Goto, M., Takahashi, R., Watanabe, T., Sugita, S., Yonemura, S., Sunagawa, G.A., et al. (2018). Establishment of immunodeficient retinal degeneration model mice and functional maturation of human ESC-derived retinal sheets after transplantation. Stem Cell Rep. 10, 1059–1074.

Janssen-Bienhold, U., Sonntag, S., Dedek, K., Dorgau, B., Schultz, K., Schmidt, K.F., Cimiotti, K., Weiler, R., Löwel, S., and Willecke, K. (2012). Ablation of retinal horizontal cells from adult mice leads to rod degeneration and remodeling in the outer retina. J. Neurosci. 32, 10713–10724.

Kruschke, J.K. (2014). Doing Bayesian data analysis: a tutorial with R, JAGS, and Stan. Phys. Rev. E.

Kuwahara, A., Ozone, C., Nakano, T., Saito, K., Eiraku, M., and Sasai, Y. (2015). Generation of a ciliary margin-like stem cell niche from self-organizing human retinal tissue. Nat. Commun. 6, 1–15.

Kuwahara, A., Yamasaki, S., Mandai, M., Watari, K., Matsushita, K., Fujiwara, M., Hori, Y., Hiramine, Y., Nukaya, D., Iwata, M., et al. (2019). Preconditioning the initial state of feeder-free human pluripotent stem cells promotes self-formation of three-dimensional retinal tissue. Sci. Rep. 9, 1–16.

Mandai, M., Fujii, M., Hashiguchi, T., Sunagawa, G.A., Ito, S., Sun, J., Kaneko, J., Sho, J., Yamada, C., and Takahashi, M. (2017). iPSC-derived retina transplants improve vision in rd1 end-stage retinal-degeneration mice. Stem Cell Rep. 8, 69–83.

Matsuyama, T., Tu, H.-Y., Sun, J., Hashiguchi, T., Akiba, R., Sho, J., Fujii, M., Onishi, A., Takahashi, M., and Mandai, M. (2021). Genetically engineered stem cell derived retinal grafts for improved retinal reconstruction after transplantation. IScience 24, 102866.

Matthews, G., and Fuchs, P. (2010). The diverse roles of ribbon synapses in sensory neurotransmission. Nat. Rev. Neurosci. 11, 812–822.

McLelland, B.T., Lin, B., Mathur, A., Aramant, R.B., Thomas, B.B., Nistor, G., Keirstead, H.S., and

Seiler, M.J. (2018). Transplanted hESC-derived retina organoid sheets differentiate, integrate, and improve visual function in retinal degenerate rats. Investig. Ophthalmol. Vis. Sci. 59, 2586–2603.

Meyer, J.S., Shearer, R.L., Capowski, E.E., Wright, L.S., Wallace, K.A., McMillan, E.L., Zhang, S.C., and Gamm, D.M. (2009). Modeling early retinal development with human embryonic and induced pluripotent stem cells. Proc. Natl. Acad. Sci. U S A 106, 16698–16703.

Nakagawa, M., Taniguchi, Y., Senda, S., Takizawa, N., Ichisaka, T., Asano, K., Morizane, A., Doi, D., Takahashi, J., Nishizawa, M., et al. (2014). A novel efficient feeder-Free culture system for the derivation of human induced pluripotent stem cells. Sci. Rep. 4, 1–7.

Nakano, T., Ando, S., Takata, N., Kawada, M., Muguruma, K., Sekiguchi, K., Saito, K., Yonemura, S., Eiraku, M., and Sasai, Y. (2012). Self-formation of optic cups and storable stratified neural retina from human ESCs. Cell Stem Cell 10, 771–785.

Palczewski, K., Van Hooser, J.P., Garwin, G.G., Chen, J., Liou, G.I., and Saari, J.C. (1999). Kinetics of visual pigment regeneration in excised mouse eyes and in mice with a targeted disruption of the gene encoding interphotoreceptor retinoid-binding protein or arrestin. Biochemistry 38, 12012–12019.

Pearson, R.A., Gonzalez-Cordero, A., West, E.L., Ribeiro, J.R., Aghaizu, N., Goh, D., Sampson, R.D., Georgiadis, A., Waldron, P.V., Duran, Y., et al. (2016). Donor and host photoreceptors engage in material transfer following transplantation of post-mitotic photoreceptor precursors. Nat. Commun. 7, 1–15.

Reichman, S., Terray, A., Slembrouck, A., Nanteau, C., Orieux, G., Habeler, W., Nandrot, E.F., Sahel, J.A., Monville, C., and Goureaua, O. (2014). From confluent human iPS cells to self-forming neural retina and retinal pigmented

epithelium. Proc. Natl. Acad. Sci. U S A *111*, 8518–8523.

Ribeiro, J., Procyk, C.A., West, E.L., O'Hara-Wright, M., Martins, M.F., Khorasani, M.M., Hare, A., Basche, M., Fernando, M., Goh, D., et al. (2021). Restoration of visual function in advanced disease after transplantation of purified human pluripotent stem cell-derived cone photoreceptors. Cell Rep. *35*, 109022.

Santos-Ferreira, T., Llonch, S., Borsch, O., Postel, K., Haas, J., and Ader, M. (2016). Retinal transplantation of photoreceptors results in donor-host cytoplasmic exchange. Nat. Commun. *7*, 1–7.

Sato, S., Omori, Y., Katoh, K., Kondo, M., Kanagawa, M., Miyata, K., Funabiki, K., Koyasu, T., Kajimura, N., Miyoshi, T., et al. (2008). Pikachurin, a dystroglycan ligand, is essential for photoreceptor ribbon synapse formation. Nat. Neurosci. *11*, 923–931.

Seiler, M.J., Aramant, R.B., Jones, M.K., Ferguson, D.L., Bryda, E.C., and Keirstead, H.S. (2014). A new immunodeficient pigmented retinal degenerate rat strain to study transplantation of human cells without immunosuppression.

Graefe's Arch. Clin. Exp. Ophthalmol. *252*, 1079–1092.

Shirai, H., Mandai, M., Matsushita, K., Kuwahara, A., Yonemura, S., Nakano, T., Assawachananont, J., Kimura, T., Saito, K., Terasaki, H., et al. (2016). Transplantation of human embryonic stem cell-derived retinal tissue in two primate models of retinal degeneration. Proc. Natl. Acad. Sci. U S A *113*, E81–E90.

Singh, M.S., Balmer, J., Barnard, A.R., Aslam, S.A., Moralli, D., Green, C.M., Barnea-Cramer, A., Duncan, I., and MacLaren, R.E. (2016). Transplanted photoreceptor precursors transfer proteins to host photoreceptors by a mechanism of cytoplasmic fusion. Nat. Commun. *7*, 1–5.

Tom Dieck, S., Altrock, W.D., Kessels, M.M., Qualmann, B., Regus, H., Brauner, D., Fejtová, A., Bracko, O., Gundelfinger, E.D., and Brandstätter, J.H. (2005). Molecular dissection of the photoreceptor ribbon synapse: physical interaction of Bassoon and RIBEYE is essential for the assembly of the ribbon complex. J. Cell Biol. *168*, 825–836.

Tu, H.Y., Watanabe, T., Shirai, H., Yamasaki, S., Kinoshita, M., Matsushita, K., Hashiguchi, T., Onoe, H., Matsuyama, T., Kuwahara, A., et al.

(2019). Medium- to long-term survival and functional examination of human iPSC-derived retinas in rat and primate models of retinal degeneration. EBioMedicine *39*, 562–574.

Wang, J.S., and Kefalov, V.J. (2011). The Cone-specific visual cycle. Prog. Retin. Eye Res. *30*, 115–128.

Yamasaki, S., Sugita, S., Horiuchi, M., Masuda, T., Fujii, S., Makabe, K., Kawasaki, A., Hayashi, T., Kuwahara, A., Kishino, A., et al. (2021). Low immunogenicity and immunosuppressive properties of human ESC- and iPSC-derived retinas. Stem Cell Rep. *16*, 851–867.

Zerti, D., Hilgen, G., Dorgau, B., Collin, J., Ader, M., Armstrong, L., Sernagor, E., and Lako, M. (2021). Transplanted pluripotent stem cell-derived photoreceptor precursors elicit conventional and unusual light responses in mice with advanced retinal degeneration. Stem Cells *39*, 882–896.

Zhong, X., Gutierrez, C., Xue, T., Hampton, C., Vergara, M.N., Cao, L.H., Peters, A., Park, T.S., Zambidis, E.T., Meyer, J.S., et al. (2014). Generation of three-dimensional retinal tissue with functional photoreceptors from human iPSCs. Nat. Commun. *5*, 1–14.

STAR★METHODS

KEY RESOURCES TABLE

REAGENT or RESOURCE	SOURCE	IDENTIFIER
Antibodies		
Goat Polyclonal anti-Arrestin 3 (Cone arrestin)	Novus Biologicals	Cat#NBP1-37003 RRID:AB_2060085
Mouse monoclonal anti-Brevican	BioLegend	Cat#820101 RRID:AB_2564837
Goat Polyclonal anti-Brn3	Santa Cruz Biotechnology	Cat#sc-6026 RRID:AB_673441
Mouse monoclonal anti-CACNA1S	Millipore	Cat#MAB427 RRID:AB_2069582
Rabbit polyclonal anti-Calbindin	Abcam	Cat#ab108404 RRID: AB_10861236
Rabbit polyclonal anti-Calretinin	Millipore	Cat#AB5054 RRID:AB_2068506
Rat monoclonal anti-CD44	Abcam	Cat#ab119348 RRID:AB_10902529
Goat polyclonal anti-Choline Acetyltransferase	Millipore	Cat#AB144P RRID:AB_2079751
Mouse monoclonal anti-Chx10	Santa Cruz Biotechnology	Cat#sc-365519 RRID:AB_10842442
Sheep polyclonal anti-Chx10	Exalpha Biologicals	Cat#X1180P RRID:AB_2314191
Mouse monoclonal anti-CNGB1	Millipore	Cat#MABN2429
Goat polyclonal anti-CNGB3	Novus Biologicals	Cat#NBP2-75087
Rabbit polyclonal anti-Crx	Takara Bio Inc.	Cat#M231
Mouse monoclonal anti-CtBP2	BD Bioscience	Cat#612044 RRID:AB_399431
Rabbit polyclonal anti-GNAT1 (Gα t1)	Santa Cruz Biotechnology	Cat#sc-389 RRID:AB_2294749
Rabbit polyclonal anti-GNAT2 (Gα t2)	Santa Cruz Biotechnology	Cat#sc-390 RRID:AB_2279097
Mouse monoclonal anti-G Protein Goα	Millipore	Cat#MAB3073 RRID:AB_94671
Rabbit polyclonal anti-GRK1	Novus Biologicals	Cat#NBP2-55226
Rabbit polyclonal anti-GUCA1A (GCAP1)	Novus Biologicals	Cat#NBP2-55158
Rabbit polyclonal anti-GUCA1B (GCAP2)	Novus Biologicals	Cat#NBP2-68721
Rabbit polyclonal anti-GUCY2D	Proteintech	Cat#55127-1-AP RRID:AB_10804281
Rabbit polyclonal anti-GUCY2F	Proteintech	Cat#25252-1-AP RRID:AB_2879989
Mouse monoclonal anti-Glutamine Synthetase (GS)	Millipore	Cat#MAB302 RRID:AB_2110656
Rabbit polyclonal anti-IMPG1	Novus Biologicals	Cat#NBP2-57461
Rabbit polyclonal anti-IMPG2	Novus Biologicals	Cat#NBP2-54954
Rabbit polyclonal anti-IRBP (RBP3)	Proteintech	Cat#14352-1-AP RRID:AB_2096956

(Continued on next page)

Continued

REAGENT or RESOURCE	SOURCE	IDENTIFIER
Mouse monoclonal anti-Islet-1	Developmental Studies Hybridoma Bank (DSHB)	Cat#40.2D6 RRID:AB_528315
Goat polyclonal anti-Islet-1	R&D Systems	Cat#AF1837 RRID:AB_2126324
Sheep polyclonal anti-Islet-2	R&D Systems	Cat#AF4244 RRID:AB_2296113
Rabbit monoclonal anti-Ku80 (human specific)	Cell Signaling Technology	Cat#2180 RRID:AB_2218736
Goat polyclonal anti-Ku80 (human specific)	R&D Systems	Cat#AF5619 RRID:AB_2218619
Rabbit polyclonal anti-L/M Opsin (Opsin, Red/Green)	Millipore	Cat#AB5405 RRID:AB_177456
Rabbit polyclonal anti-LRIT3	Novus Biologicals	Cat#NBP1-83895 RRID:AB_11039569
Rabbit polyclonal anti-L7/Pcp2	Takara Bio Inc.	Cat#M202
Rabbit polyclonal anti-mGluR6	Novus Biologicals	Cat#NLS4655 RRID:AB_343723
Mouse monoclonal anti-Nanog	Millipore	Cat#MABD24 RRID:AB_11203826
Rabbit polyclonal anti-Oct3/4	Santa Cruz Biotechnology	Cat#sc-9081 RRID:AB_2167703
Mouse monoclonal anti-Pax6	BD Pharmingen	Cat#561462 RRID:AB_10715442
Rabbit polyclonal anti-PDE6α	Novus Biologicals	Cat#NBP1-87312 RRID:AB_11009970
Rabbit polyclonal anti-PDE6β	Novus Biologicals	Cat#NB120-5663 RRID:AB_792693
Rabbit polyclonal anti-PDE6H	Novus Biologicals	Cat#NBP2-68659
Rabbit polyclonal anti-Pikachurin	Abcam	Cat#ab91314 RRID:AB_10861100
Mouse-monoclonal anti-PKCα	Novus Biologicals	Cat#NB600-201 RRID:AB_10003372
Goat polyclonal anti-PKCα	R&D Systems	Cat#AF5340 RRID:AB_2168552
Lectin peanut agglutinin (PNA), Alexa Fluor 647 conjugate	Thermo Fisher Scientific	Cat#L32460
Mouse monoclonal anti-Peripherin-2 (PRPH2)	Millipore	Cat#MABN293
Rabbit polyclonal anti-Peripherin-2 (PRPH2)	Proteintech	Cat#18109-1-AP RRID:AB_10665364
Mouse monoclonal anti-PSD95	BioLegend	Cat#810401 RRID:AB_2564750
Mouse monoclonal anti-RBPMS	Novus Biologicals	Cat#NBP2-45551
Rabbit polyclonal anti-Recoverin	Proteintech	Cat#10073-1-AP RRID:AB_2178005
Mouse monoclonal anti-Rhodopsin	Millipore	Cat#MABN15 RRID:AB_10807045
Mouse monoclonal anti-Rxrγ	Santa Cruz Biotechnology	Cat#sc-365252 RRID:AB_10850062

(Continued on next page)

Continued

REAGENT or RESOURCE	SOURCE	IDENTIFIER
Mouse monoclonal anti-S arrestin	Novus Biologicals	Cat#NBP2-25161
Sheep polyclonal anti-Secretagogin	BioVendor	Cat#RD184120100 RRID:AB_2034062
Goat polyclonal anti-S-Opsin (Opsin, Blue)	Santa Cruz Biotechnology	Cat#sc-14363 RRID:AB_2158332
Mouse monoclonal anti-Stem123 (human specific GFAP)	Takara Bio Inc.	Cat#Y40420 RRID:AB_2833249
Goat polyclonal anti-Synaptophysin	R&D Systems	Cat#AF5555 RRID:AB_2198864
Mouse monoclonal anti-Versican	Millipore	Cat#MABT161
Alexa Fluor 488 Donkey Anti-Mouse IgG (H+L)	Thermo Fisher Scientific	Cat#A21202 RRID:AB_141607
Alexa Fluor 546 Donkey Anti-Mouse IgG (H+L)	Thermo Fisher Scientific	Cat#A10036 RRID:AB_2534012
Alexa Fluor 647 Donkey Anti-Mouse IgG (H+L)	Thermo Fisher Scientific	Cat#A31571 RRID:AB_162542
Alexa Fluor 488 Donkey Anti-Rabbit IgG (H+L)	Thermo Fisher Scientific	Cat#A21206 RRID:AB_2535792
Alexa Fluor 546 Donkey Anti-Rabbit IgG (H+L)	Thermo Fisher Scientific	Cat#A10040 RRID:AB_2534016
Alexa Fluor 647 Donkey Anti-Rabbit IgG (H+L)	Thermo Fisher Scientific	Cat#A31573 RRID:AB_2536183
Alexa Fluor 488 Goat Anti-Mouse IgM (H+L)	Thermo Fisher Scientific	Cat#A10680 RRID:AB_2534062
Alexa Fluor 546 Donkey Anti-Sheep IgG (H+L)	Thermo Fisher Scientific	Cat#A21098 RRID:AB_2535752
Alexa Fluor 647 Donkey Anti-Goat IgG (H+L)	Thermo Fisher Scientific	Cat#A21447 RRID:AB_2535864
Mouse monoclonal anti-Chx10, Alexa Fluor 647 conjugate	Santa Cruz Biotechnology	Cat#sc-365519 AF647 RRID:AB_10842442
Mouse monoclonal anti-Islet-1, PE conjugate	BD Biosciences	Cat#562547 RRID:AB_11154592
Mouse monoclonal anti-Ki67, Alexa Fluor 647 conjugate	BD Biosciences	Cat#558615 RRID:AB_647130
Mouse monoclonal anti-Nrl, Alexa Fluor 647 conjugate	Santa Cruz Biotechnology	Cat#sc-374277 AF647 RRID:AB_10991100
Mouse monoclonal anti-Pax6, Alexa Fluor 647 conjugate	BD Biosciences	Cat#562249 RRID:AB_11152956
Mouse monoclonal anti-RXRγ, Alexa Fluor 647 conjugate	Santa Cruz Biotechnology	Cat#sc-365252 AF647 RRID:AB_10850062
Mouse monoclonal anti-Sox2, BV421 conjugate	BioLegend	Cat#656114 RRID:AB_2566262
Mouse IgG1κ Isotype control, APC conjugate	BioLegend	Cat#400120 RRID:AB_2888687
Mouse IgG2aκ Isotype control, APC conjugate	BioLegend	Cat#400220 RRID:AB_326468
Chemicals, peptides, and recombinant proteins		
Knockout Serum Replacement	Thermo Fisher Scientific	Cat#10828-028
FBS	Thermo Fisher Scientific	Cat#10270-106

(Continued on next page)

Continued

REAGENT or RESOURCE	SOURCE	IDENTIFIER
N2-Supplement	Thermo Fisher Scientific	Cat#17502-048
LM511-E8 matrix	Matrixome	Cat#892011
Y-27632	Wako Pure Chemical Industries, Ltd.	Cat#039-24591
SB431542	Sigma-Aldrich	Cat#S4317
SAG	Enzo Biochem Inc.	Cat#ALX-270-M001
BMP4	R&D Systems	Cat#314-BP-050
GSK-3 Inhibitor XVI(CHIR99021)	Wako Pure Chemical Industries, Ltd.	Cat#038-24681
SU5402	Wako Pure Chemical Industries, Ltd	Cat#197-16731
Neuron Dissociation Solution S	Wako Pure Chemical Industries, Ltd	Cat#297-78101
Stem Fit AK03N	Ajinomoto	Cat#AK03N
DMEM/F-12 Glutamax	Thermo Fisher Scientific	Cat#10565-018
IMDM GlutaMAX	Thermo Fisher Scientific	Cat#31980-097
Ham's F-12 Nutrient Mixture	Thermo Fisher Scientific	Cat#11765-062
CD lipid concentrate	Thermo Fisher Scientific	Cat#11905-031
1-thioglycerol	Sigma-Aldrich	Cat#M6145
DMSO	Wako Pure Chemical Industries, Ltd	Cat#037-24053
citrate buffer	Thermo Fisher Scientific	Cat#AP-9003-125
4% paraformaldehyde (PFA)	Wako Pure Chemical Industries, Ltd	Cat#30525-89-4
4′,6-Diamidino-2-phenylindole, dihydrochloride (DAPI)	Thermo Fisher Scientific	Cat#D1306
bovine serum albumin	Sigma-Aldrich	Cat#A4161
L-AP4	Wako Pure Chemical Industries, Ltd	Cat#016-22083
Opsinamide	Sigma-Aldrich	Cat#AA92593
Critical commercial assays		
Human Stem Cell Nucleofector™ Kit	Lonza	Cat#VPH-5012
Experimental models: Cell lines		
KhES1 *Crx::*Venus reporter line	Nakano et al., 2012	HES0653
Ilset-1⁻/⁻KhES1 *Crx::*Venus reporter line	This paper	N/A
Experimental models: Organisms/strains		
SD-Foxn1 Tg (S334ter) 3LavRrrc nude rats	Rat Research Resource Center	RRRC# 539
Software and algorithms		
CED spike 2 (version 7.2)	CED	NA
MC_Rack	Multi Channel System	https://www.multichannelsystems.com/software/mc-rack
FlowJo v10	BD	http://www.flowjo.com/
Fiji/ImageJ	National Institutes of Health (NIH)	http://figi.sc
IMARIS 8.4	Oxford Instruments	https://imaris.oxinst.com
R	R Core Team, 2020	https://cran.r-project.org
ZEN imaging software (blue edition)	Carl Zeiss	https://www.zeiss.de/mikroskopie/produkte/mikroskopsoftware/zen-lite.html
Code (stan) for statistical analyses	Github	https://github.com/matsutakehoyo/KO-graft
Other		
USB-MEA60-up-system	Multi channel Systems	NA
Nucleofector™ 2b	Lonza	Cat#AAB-100

RESOURCE AVAILABILITY

Lead contact

Further information and requests for resources and reagents should be directed to and will be fulfilled by the lead contact, Michiko Mandai (michiko.mandai@riken.jp).

Materials availability

Materials generated in this study are available from the lead contact's laboratory upon request.

Data and code availability

- The code used for statistical analyses is available in a github repository (https://github.com/matsutakehoyo/KO-graft).

- The datasets supporting the current study have not been deposited in a public repository because of the large size of the data but are available from the corresponding author on request.

- Any additional information required to reanalyze the data reported in this paper is available from the lead contact upon reasonable request.

EXPERIMENTAL MODEL AND SUBJECT DETAILS

Human ES cell line

hESC (KhES-1) line (RIKEN BioResource Center, Cell Number: HES0653) was used in accordance with hESC research guidelines of the Japanese government. hESCs express Venus under the control of Crx promoter (Nakano et al., 2012).

Rat model

SD-Foxn1 Tg (S334ter) 3LavRrrc nude rats were obtained from the Rat Resource and Research Center for transplantation study (Seiler et al., 2014).

Animal transplantation experiments were performed in accordance with local guidelines and the ARVO statement on the use of animals in ophthalmic and vision research. All experimental protocols were approved by the RIKEN Biosystems Dynamics Research Ethics Committee and were conducted according to guidelines for animal experiments of the RIKEN. Rats of 16-25 postnatal weeks were used for transplantation. MEA data was analyzed using a total of 31 rats (14 males and 17 females) after transplantation. Among these, 22–23 transplanted retinas were also used for quantitative analysis by immunohistology.

METHOD DETAILS

Establishment of $ISL1^{-/-}$ hESC line

hESCs were maintained using iMatrix511 (Matrixome) and Stem fit (AK03N, Ajinomoto, Japan) feeder free culture (Nakagawa et al., 2014). The Cas9 and puromycin-resistance gene bearing plasmid pSpCas9(BB)-2A-Puro (Addgene), with a pair of CRISPR/Cas9 guide RNAs designed so as to delete the first and second exons of the $ISL1$ gene (Sequence ID: CCAACTCCGCCGGCTTAAAT, GGGAGGTTAATACTTCGGAG), was transfected to the hESCs by electroporation (Nucleofector IIb, program B-016, Lonza). Transfected hESCs were cultured in a six-well plate (1.0×10^3 cells per well; AGC Techno Glass, Japan) coated with iMatrix511 in the presence of 10 μM Y-27632 (ROCK inhibitor, Wako Pure Chemical Industries, Japan) in Stem Fit. One day after inoculation, the medium was replaced without Y-27632. Thereafter, the hESCs were cultured for six days in the presence of 0.5 ng/mL puromycin for puromycin selection. The successfully transfected colonies were picked up and the genomic DNA was analyzed using PCR primers designed around the target site. We then established two clones with $ISL1$ gene deletion (No. 330A16 line and No. 330A19 line). $ISL1$ gene-deleted hESC clones were analyzed by Sanger sequencing to confirm disruption of the $ISL1$ gene.

Retinal differentiation and long-term culture

Retinal differentiation was conducted following the modified SFEBq method we recently reported (Kuwahara et al., 2019; Yamasaki et al., 2021) (Nukaya et al.; WO19/017,492, 054,514, 054,515). In brief, subconfluent hESCs were treated with 5 μM SB431542 (TGFβ receptor inhibitor, Sigma-Aldrich) and 300 nM SAG (Smoothened agonist, Enzo Biochem) from 24 h prior to differentiation. Cells were then dissociated into

single cells using TrypLE Select Enzyme (Thermo Fisher Scientific), suspended in 100 μL serum-free culture medium with 10 μM Y-27632, and cultured at 1.2×10^4 cells per well in low cell adhesion 96-well V-bottomed plates (Sumitomo Bakelite). On differentiation day (DD) 3 after initiation of suspension culture, aggregates were treated with 1.5 nM recombinant human BMP4 protein (R&D Systems). Aggregates on DD14 were transitioned to RPE induction medium with 3 μM CHIR99021 (GSK3β inhibitor, Wako Pure Chemical Industries) and 5 nM SU5402 (FGF signaling pathway inhibitor, Wako Pure Chemical Industries) for 3–4 days in a 90-mm low adhesion culture dish (Sumitomo Bakelite). Subsequently, aggregates were cultured in the maturation culture (Yamasaki et al., 2021) (Nukaya et al. in preparation; WO2019017492A1, WO2019054514A1). The medium was exchanged every 3–4 days.

Flow cytometry

The differentiated retinal cell population was analyzed by staining the intracellular markers for each retinal neuron type. hESC-retina was dissociated using Neuron Dissociation Solution (Wako Pure Chemical Industries) (20-30 min at 37°C) followed by a repeated wash with PBS, and dissociated cells were fixed using Fixation/Permeabilization Solution Kit (BD Biosciences) or transcription factor buffer Kit (BD Biosciences) at 4°C for 20 min. Cells were permeabilized with Perm/Wash buffer, centrifuged, and resuspended in Perm/Wash buffer for a reaction with BV421- or Alexa Fluor 647-conjugated antibodies for 60 min at 4°C. For some antibodies without conjugated fluorochrome, the second antibody was applied at 4°C for 60 min. Then cells were washed twice with Perm/Wash buffer and resuspended in 2% FBS/PBS buffer for FCM analysis using FACS Canto II (BD Biosciences). The antibodies used in this analysis are listed in key resources table. FCM data were analyzed using FlowJo software (BD Biosciences).

Transplantation into retinal degeneration model nude rats

For graft preparation, hESC-retinas were cut into small pieces of approximately 0.5 mm width, indicated by *Crx::Venus*[+] fluorescence, using micro scissors. Before transplantation surgery, nude rats with retinal degeneration at 16–25 postnatal weeks were anesthetized with ketamine hydrochloride (40–80 mg/kg) and Xylazine (5–10 mg/kg), or by inhalation of 3–5% isoflurane. Pupils were dilated using MydrinP (Santen Pharmaceutical, Japan). The glass capillary (1-000-0500, Drummon, Alabama, USA) for transplantation was pulled with the P-97/IVF puller (SUTTER INSTRUMENT, California, USA), followed by cutting and sharpening using a microgrinder (EG-400, Narishige, Tokyo, Japan). The glass capillary was attached to the microelectrode holder (MPH310, World Precision Instruments., FL, USA) on a 6.3 mm electrode handle (2505, World Precision Instruments.), connected to a 10 μL micro-syringe (1701LT, Hamilton, MA, USA) with an extension tube. hESC-retinas were loaded into the capillary tip and gently transplanted into the subretinal space of rats under a surgical microscope.

Multi-electrode array (MEA) recording

Nude rats transplanted with hESC-retina were used for multi-electrode array (MEA) recording at 14–15 months old (i.e., 8–10 months after transplantation). The procedure of MEA recording with a USB-MEA60-Up-System (Multi Channel Systems) and offline spike sorting are described in detail below (Matsuyama et al., 2021; Tu et al., 2019). Rats were dark-adapted for 1–3 days before dissection under a dim red LED that peaked at a wavelength of 700 nm. Isoflurane or sevoflurane inhalation was used for both initial anesthetization and overdose euthanasia. The freshly harvested eyecups were kept in oxygenated Ames' medium (Sigma-Aldrich) constantly supplied with 95% O_2 and 5% CO_2 in the dark until use. The retina was carefully isolated from the sclera and the graft was identified at the subretinal side by its voluminous, spotted appearance. After removing the residual vitreous, the retina was minimally trimmed to keep its integrity and immediately mounted with the RGC side down and the grafted area centered on the electrode area. From then, the retina was constantly supplied with oxygenated Ames' medium perfused at 3–3.5 mL/min. The retina was allowed to recover for at least 20 min. Full-field light stimulation at different intensities (weak: 10.56, medium: 12.16, strong: 12.84 log photons/cm²/s) was generated with a white LED (NSPW500C, Nichia Corp., Tokushima, Japan) without background illumination. Each 20 s recording with 1 s stimulation in the middle was repeated three times as a set, and each set of stimulation was repeated before, during and after the 10 μM L-AP4 (agonistic blocker mGluR6, Wako Pure Chemical Industries) treatment. Much brighter stimulation at 15.48 log photons/cm²/s (super-strong) was applied only at the very end of each experiment for each sample for retinal viability confirmation. To suppress the intrinsic photosensitivity of melanopsin expressing cells, 10 μM opsinamide (Opn4 Antagonist; Sigma-Aldrich) was added to the perfusion medium from the beginning of preparation. After recording, the retina was harvested and fixed with 4% PFA at room temperature for immunohistochemistry.

MEA data were collected at a 20 kHz sampling rate without applying a filter. Recorded spikes were sorted offline, using the automatic template formation and spike matching algorithm of Spike 2 (version 7.2, CED) with a few minor modifications, including a −20 μV threshold, a 5% tolerance for maximal amplitude change, and a Butterworth band-pass filter (200-2800Hz) together with DC offset removal. Recordings with the same stimulus intensity taken before, during and after L-AP4 treatment were merged to follow the spike trains from the same set of cells during the 3–4 h recording of each sample. The detected cells (i.e., spike sources) were then categorized into *unresponsive*, *onXoff*, *on* and *adapted on* types (see also Figure 6F) according to their light response pattern during the whole recording procedure.

Immunohistochemistry (IHC)

WT and *ISL1*$^{-/-}$ hESC-retinas and transplanted retinas were fixed in 4% paraformaldehyde at 4°C for 15–60 min and cryoprotected in 30% sucrose/PBS overnight. After MEA recording, transplanted retinas were fixed in 4% paraformaldehyde for 15 min at room temperature for cryo-section immunostaining. hESC-retinas were embedded in OCT compound (Sakura Finetek Japan) and sectioned at 12 μm thickness. Sections were washed with 0.3% Triton X-100/PBS prior to heat-induced epitope retrieval using citrate buffer (Thermo Fisher Scientific) and blocked in 3% BSA/0.3% Triton X-100/PBS for 1 h at room temperature. Primary antibodies diluted in 3% BSA/ 0.3% Triton X-100/PBS were incubated at 4°C overnight, followed by secondary antibodies for 1 h at room temperature together with DAPI. Tertiary antibodies such as Alexa Fluor 488-conjugated Ku80 were then applied after washing with 0.05% Tween/PBS. All images were obtained using BZX810 (Keyence) fluorescence microscopy, TCS SP-8 (Leica Camera) or LSM880 (Carl Zeiss) laser scanning confocal microscopes, and offline processed using IMARIS and Zen Blue (Carl Zeiss) imaging software.

Quantification analysis

For immunohistological features, host-graft contact and IS/OS patterns were quantified based on the categorization indicated in the figures and text, by observing 6–67 rosettes in 1–7 images for each sample. ChAT analysis to determine IPL preservation was assessed in the area over the graft rosettes by observing 5–50 rosettes in 1–6 images for each sample.

Statistical analysis

We used full Bayesian statistical inference with MCMC sampling for statistical modeling using Rstan (Stan Development Team. 2017. RStan: the R interface to Stan. R package version 2.16.2. http://mc-stan.org). Our data are multi-dimensional with a natural hierarchical structure, with observations having multiple possible predictors, such as group (control, WT, and KO (*ISL1*$^{-/-}$)) effects, sex (female or male) effects, inter-sample variation, and other predictors. We estimated the distribution of these effects using hierarchical Bayesian linear regression models. Note that posterior estimates do not represent a simple pooling of data for a particular set of predictor combinations (for example comparing population means); rather they represent the effect of predictors while considering the data as a whole.

We show the posterior distributions of parameters, which indicate the probability for the value of the parameter given the data, with 95% compatibility intervals (confidence intervals) and mean indicated above. Whenever a possible effect or difference between parameters is indicated we estimate the magnitude and credibility of the effect from the distribution of the difference between parameter values. Whenever a difference is indicated we therefore indicate the fraction of the area over zero, which indicates the confidence that we have that there is a difference. Stan scripts for the models are provided in a GitHub repository (https://github.com/matsutakehoyo/KO-graft).

Analysis of rosette contact, IPL preservation, and OS elongation. Rosette contact, host IPL preservation, and photoreceptor OS elongation were quantified using an ordinal scale with three categories (for example bad, poor, fair). We estimated the effects of different predictors assuming an underlying metric variable with a normal distribution following (Kruschke, J. *Doing Bayesian data analysis: A tutorial with R, JAGS, and Stan. Physical Review E* **70**, (2014).). Since there are only three categories, we fixed the cutoff intervals to 1.5 and 2.5 and estimated the mean and standard deviation of the underlaying metric variable.

Thus, the category for each observation y_i is described by

$$y_i \sim Categorical(\gamma_1,\ \gamma_2, \gamma_3)$$

$$\gamma_{1,i} = p(\gamma = 1,\ \mu_i,\ \sigma) = \Phi\left(\frac{1.5 - \mu_i}{\sigma}\right)$$

$$\gamma_{2,i} = (\gamma = 2,\ \mu_i, \sigma) = \Phi\left(\frac{2.5 - \mu_i}{\sigma}\right) - \Phi\left(\frac{1.5 - \mu_i}{\sigma}\right)$$

$$\gamma_3 = p(\gamma = 3, \mu_i,\ \sigma,\ \theta_2) = 1 - \Phi\left(\frac{2.5 - \mu_i}{\sigma}\right)$$

$$\mu_i = \beta_0 + \beta_{grp} + \beta_{sex} + \beta_{smp}$$

Where γ_k $k \in \{1, 2, 3\}$ represent the probability of observing each of the categories ($\sum \gamma = 1$). γ_1 correspond to the area under the normal to the left of 1.5, γ_2 is the area of the curve between 1.5 and 2.5, and γ_3 is the area of the normal to the right of 2.5. μ and σ represent the mean and the standard deviation of the underlaying metric variable. We assume equal standard variation across predictors for simplicity, however, we note that similar results were obtained with models where the effects of different predictors on the standard deviation were taken into account. β_0 represents the overall mean, and the effects of different predictors were calculated as a deviation from this mean with the sum-to-zero constraint on each of the predictors (($\sum \beta_{predictor} = 0$)). For the effect of the sample we estimated hyperparameters from the data; otherwise we used generic weakly informative priors (Normal(0,1)) for predictors. So for β

$$\beta_{grp} \sim Normal(0, 1)$$
$$\beta_{sex} \sim Normal(0, 1)$$
$$\beta_{smp} \sim Normal(0, \sigma_{smp})$$
$$\sigma_{smp} \sim Normal(0, 1)$$
$$\sigma \sim Normal(0, 1)$$

RGC spontaneous firing (9 s recording before the 1 s stimuli). We analyzed the distribution of spontaneous firing, by calculating the spontaneous firing rate before light stimulation (9 s). The distribution of spontaneous firing rate closely follows a lognormal distribution, as shown in Figure 6. We therefore modeled the influence of parameters on the mean log spontaneous firing. For the spontaneous firing analysis, we used 60396 observations from 23828 cells collected across 47 retinas. The number of observations in this analysis is higher than the number in the light response analysis, as we consider the spontaneous activity before, during, and after L-AP4 treatment, in addition to the different stimuli.

The spontaneous firing rate is then described by

$$y_i \sim lognormal(\mu_i, \sigma)$$
$$\mu_i = \mu_0 + \mu_{grp} + \mu_{sex} + \mu_{cnd} + \mu_{stm} + \mu_{smp}$$
$$grp \in \{control,\ WT,\ KO\}$$
$$sex \in \{female,\ male\}$$
$$cnd \in \{before,\ L-AP4,\ after\}$$
$$stm \in \{weak,\ medium,\ strong\}$$

where y_i is the log spontaneous firing rate for a particular observation i. μ_0 and σ are the overall logmean and logsd of the lognormal distribution. We assume a common σ to simplify the model. The effects of different predictors were calculated as a deviation from this mean with the sum-to-zero constraint on each of the predictors ($\sum \mu_{predictor} = 0$).

We used a flat prior for σ and a vague prior derived from the data for the overall mean (μ_0).

$$\mu_0 \sim Normal\left(\log(\overline{y}), 1\right)$$
$$\sigma \sim Uniform(0, Inf)$$

For the effect of sample, we estimated the hyperparameter (σ_{smp}) from the data; otherwise we used generic weakly informative priors (Normal(0, 1)).

$$\mu_{grp} \sim Normal(0, 1)$$
$$\mu_{sex} \sim Normal(0, 1)$$
$$\mu_{cnd} \sim Normal(0, 1)$$

$$\mu_{\text{stm}} \sim Normal(0, 1)$$
$$\mu_{\text{smp}} \sim Normal(0, \sigma_{\text{smp}})$$
$$\sigma_{\text{smp}} \sim Normal(0, 1)$$

RGC response probability.   The response types to a 1 s stimulus for each cell in each condition were first described as unresponsive, transient ON, sustained ON, delayed ON, ON suppression, OFF, ON-OFF and hypersensitive separately (see also Matsuyama et al., 2021), by comparing the onset and termination timing of their spiking frequency changes in response to the stimulation. Cells were then grouped as "*!light*" (*unresponsive*), "*on*", "*adapted on*" or "*onXoff*" types based on their response patterns across all three conditions (before, during and after L-AP4). In principle, "*on*" cells showed L-AP4 sensitive ON (including sustained ON) responses throughout the whole recording, while "*adapted on*" cells had their ON responses (mostly sustained ON) seen only after recovery from L-AP4. Although cells with OFF responses were also included, the rarely found "*onXoff*" type mostly consists of cells showing ON and OFF responses that were both sensitive to L-AP4 blockade, suggesting an ON-dependent OFF pathway involvement in the synaptic inputs to these cells. Note that delayed ON and hypersensitive responses were seldom observed and proved independent of the synaptic inputs; they were therefore assigned to the "*!light*" *unresponsive* type. Responses that were not consistent across the three replicate recordings were disregarded.

We collected 19,662 observations from 19,662 cells collected across 47 retinas. Note that responses from the same set of cells to different stimulus strengths are treated as different cells. We then modeled the probability that cells would produce a light response (either *on*, *onXoff* or *adapted on*) using robust logistic regression. The probability of observing a light response y_i is

$$y_i \sim Bernoulli(\theta_i)$$
$$\theta_i = \frac{1}{2} guess + (1 - guess)\log istic\left(\beta_0 + \beta_{\text{grp}} + \beta_{\text{stm}} + \beta_{\text{sex}} + \beta_{\text{smp}} + \beta_{\text{spt}} * f_i\right)$$
$$grp \in \{control, \ WT, \ KO\}$$
$$sex \in \{female, \ male\}$$
$$stm \in \{weak, \ medium, \ strong\}$$

where y_i is either 0 (no light response) or 1 (light responsive) and θ_i is the probability that the cell will respond to the light stimulus. β_0 represents the overall mean and the effects of different predictors were calculated as a deviation from this mean with the sum-to-zero constraint on each of the predictors ($\sum \beta_{[predictor]} = 0$). β_{spt} representing the effect of spontaneous firing, and f_i the spontaneous firing rate of each cell. The spontaneous firing rate during L-AP4 treatment was taken as the most representative value for the cell spontaneous frequency, as this condition represents the cells' firing without input from the outer retina.

The prior for the overall mean (β_0) was estimated from the data (in log odds, probability of response: $p_{\neq 0}$) with sd of 1.

$$\beta_0 \sim Normal(logit(p_{\neq 0}), \ 1)$$

For the effect of the sample, we estimated the hyperparameter (σ_{smp}) from the data, otherwise we used generic weakly informative priors ($Normal(0, 1)$).

$$\beta_{\text{grp}} \sim Normal(0, 1)$$
$$\beta_{\text{sex}} \sim Normal(0, 1)$$
$$\beta_{\text{stm}} \sim Normal(0, 1)$$
$$\mu_{\text{smp}} \sim Normal(0, \sigma_{\text{smp}})$$
$$\sigma_{\text{smp}} \sim Normal(0, 1)$$

For the guess parameter, which represents outliers, we followed the recommendation from Kruschke (Kruschke, 2014) for robust logistic regression (Chapter 21.3). Using *Beta*(1, 9) which emphasizes small values, reflecting our expectation that the proportion of outliers is small. In particular, *Beta*(1, 9) gives values greater than 0.5 a very small but non-zero probability.

$$guess \sim Beta(1, 9)$$

Feature correlation analysis. Correlation among RGC spontaneous activity, RGC light responsiveness, rosette contact, photoreceptor OS elongation, and IPL preservation was analyzed by extending Pearson's correlation test to a Bayesian framework. We used sample estimates from the respective analyses and estimated their correlation assuming a bivariate distribution. A total of 21 samples, where information was available for all the analyzed features, was used for this analysis. For the bivariate distribution we used the Student's t distribution instead of the normal distribution and estimated the degrees of freedom ν from the data to implement robustness.

$$x \sim MultiStudent\_t(\nu, \mu, \Sigma)$$

The correlation and standard deviation between two features is given by the Variance-Covariance matrix Σ, which was estimated by Cholesky decomposition

$$\Sigma = LRL$$

where L is the diagonal matrix with standard deviations (σ) and R is the correlation matrix. R is further decomposed to two triangular matrices

$$R = L_{corr} * L_{corr}^{T}$$

For the mean and standard deviations we used weakly informative priors.

$$\mu \sim Normal(0, 1)$$
$$\sigma \sim Normal(0, 1)$$

For the correlation matrix we used the LKJ correlation distribution with $\eta = 2$ which is moderately skeptical of extreme correlations near -1 or 1.

$$L_{corr} \sim LKJcorr(2)$$

We followed Stan's recommendations for the degrees of freedom of the Student's t distribution.

$$\nu \sim Gamma(2, 0.1)$$